BRNO UNIVERSITY OF TECHNOLOGY
VYSOKÉ UČENÍ TECHNICKÉ V BRNĚ

FACULTY OF MECHANICAL ENGINEERING
INSTITUTE OF PHYSICAL ENGINEERING

FAKULTA STROJNÍHO INŽENÝRSTVÍ
ÚSTAV FYZIKÁLNÍHO INŽENÝRSTVÍ

ELECTROSTATIC DEFLECTION AND CORRECTION SYSTEMS

MASTER'S THESIS
DIPLOMOVÁ PRÁCE

AUTHOR Bc. VIKTOR BADIN
AUTOR PRÁCE

Brno 2015

BRNO UNIVERSITY OF TECHNOLOGY
VYSOKÉ UČENÍ TECHNICKÉ V BRNĚ

FACULTY OF MECHANICAL ENGINEERING
INSTITUTE OF PHYSICAL ENGINEERING

FAKULTA STROJNÍHO INŽENÝRSTVÍ
ÚSTAV FYZIKÁLNÍHO INŽENÝRSTVÍ

ELECTROSTATIC DEFLECTION AND CORRECTION SYSTEMS

ELEKTROSTATICKÉ VYCHYLOVACÍ A KOREKČNÍ SYSTÉMY

MASTER'S THESIS
DIPLOMOVÁ PRÁCE

AUTHOR
AUTOR PRÁCE

Bc. VIKTOR BADIN

SUPERVISOR
VEDOUCÍ PRÁCE

Ing. JAKUB ZLÁMAL, Ph.D.

BRNO 2015

Vysoké učení technické v Brně, Fakulta strojního inženýrství

Ústav fyzikálního inženýrství
Akademický rok: 2014/2015

ZADÁNÍ DIPLOMOVÉ PRÁCE

student(ka): Bc. Viktor Badin

který/která studuje v **magisterském navazujícím studijním programu**

obor: **Fyzikální inženýrství a nanotechnologie (3901T043)**

Ředitel ústavu Vám v souladu se zákonem č.111/1998 o vysokých školách a se Studijním a zkušebním řádem VUT v Brně určuje následující téma diplomové práce:

Elektrostatické vychylovací a korekční systémy

v anglickém jazyce:

Electrostatic Deflection and Correction Systems

Stručná charakteristika problematiky úkolu:

Prozkoumat možnosti elektrostatického vychylování a dynamické fokusace.

Cíle diplomové práce:

Určit citlivost dynamické fokusace a stigmování pro ELG s Gaussovským svazkem. Ilustrovat na příkladu čoček ELG 600 (objektiv a poslední kondenzor), doplněný o elektrostatický vychylovací systém a jeho porovnání s existujícím magnetickým systémem. Slabá elektrostatická čočka ve zmenšovacím kondenzoru se může použít pro dynamickou fokusaci (posuv křižiště tak, aby po vychýlení byla stopa ostrá). Jaká geometrie je nejvhodnější pro tuto čočku, jaká je její účinnost? Jak funguje dynamický stigmátor a jak ovlivňuje zkreslení vychylovacího systému?

Seznam odborné literatury:

[1] B. Lencová, kandidátská dizertace, Brno 1988

[2] Brodie and J. J. Muray, The Physics of Micro / Nano-Fabrication, Plenum Press, NY 2010

Vedoucí diplomové práce:Ing. Jakub Zlámal, Ph.D.

Termín odevzdání diplomové práce je stanoven časovým plánem akademického roku 2014/15.

V Brně, dne 21. 11. 2014

L.S.

VYSOKÉ UČENÍ TECHNICKÉ V BRNĚ
FAKULTA STROJNÍHO INŽENÝRSTVÍ
DĚKANÁT
5

prof. RNDr. Tomáš Šikola, CSc.
ředitel ústavu

doc. Ing. Jaroslav Katolický, Ph.D.
děkan

ABSTRACT
The aim of this master's thesis is to explore and study the possibilities of dynamic correction of aberrations in electron-beam lithography systems. For the calculations, the optical column of the Tesla BS600 series electron-beam writer was used. The thesis focuses on corrections of the third order field curvature, astigmatism, and distortion aberrations of the currently used magnetic deflection system and a newly designed electrostatic deflection system and stigmator. The parameters of the two deflection and correction systems were compared.

KEYWORDS
Electron-beam lithography, aberrations, charged particle optics, dynamic aberration correction, field curvature, astigmatism, distortion.

ABSTRAKT
Tato diplomová práce se věnuje prozkoumání možností dynamické korekce vad v elektronové litografii. Pro výpočty byl zvolen elektronový litograf Tesla BS600. Práce se zabývá korekcí vad vychýlení třetího řádu: zklenutí pole, astigmatismu a zkreslení. Aberace byly spočteny jak pro současný magnetický vychylovací systém, tak pro nově navržený elektrostatický deflektor a stigmátor. Vlastnosti a vady obou vychylovacích a korekčních systémů byly porovnány.

KLÍČOVÁ SLOVA
Elektronová litografie, vady zobrazení, optika nabitých částic, dynamická korekce vad, zklenutí pole, astigmatismus, zkreslení.

BADIN, Viktor *Electrostatic Deflection and Correction Systems*: master's thesis. Brno: Brno University of Technology, Faculty of Mechanical Engineering, Institute of Physical Engineering, 2015. 78 p. Supervised by Ing. Jakub Zlámal, Ph.D.

DECLARATION

I declare that I have written my master's thesis on the theme of "Electrostatic Deflection and Correction Systems" independently, under the guidance of the master's thesis supervisor and using the technical literature and other sources of information which are all quoted in the thesis and detailed in the list of literature at the end of the thesis.

As the author of the master's thesis I furthermore declare that, as regards the creation of this master's thesis, I have not infringed any copyright. In particular, I have not unlawfully encroached on anyone's personal and/or ownership rights and I am fully aware of the consequences in the case of breaking Regulation § 11 and the following of the Copyright Act No 121/2000 Sb., and of the rights related to intellectual property right and changes in some Acts (Intellectual Property Act) and formulated in later regulations, inclusive of the possible consequences resulting from the provisions of Criminal Act No 40/2009 Sb., Section 2, Head VI, Part 4.

Brno . . . .

(author's signature)

ACKNOWLEDGEMENT

First and foremost, I would like to thank my supervisor Ing. Jakub Zlámal, Ph.D. for the fruitful consultations and his countless hours spent on helping me with my thesis. A huge thank you to my family and friends, and to everyone who made my student life so joyful.

CONTENTS

INTRODUCTION

Electron-beam lithography systems have been used extensively in the past decades in both research and high-end commercial applications. Electron-beam lithography is one of the few methods allowing nanometer-scale patterning and is therefore essential in many modern fields such as nanotechnology. Direct-write electron-beam machines have a huge advantage that they can write almost arbitrary patterns without a requiring masks. This makes them a very powerful tool especially in research fields, prototyping, etc. Their versatility comes at a price — low writing speed for complex patterns and the write field is limited by electron-optical aberrations. The small write field needs to be compensated by mechanically moving the patterned substrate during exposure leading to stitching errors and longer processing times. The needed high precision translation stages greatly increase the price of lithography. The aberrations can never be eliminated completely. They can be usually lowered by skillful design of the beam optics. Another possibility of lowering aberrations is introducing dynamic correction devices which have aberrations of their own and can be made to cancel the inherent aberrations of the beam deflection system, for example. Wider write fields are then possible reducing the overhead in large scale electron-beam patterning and effectively increasing throughput. Studying the possibilities of dynamic aberration correction in electron-beam lithography is the main goal of this thesis.

The first part of the thesis offers an introduction into the physics and mathematics of charged particle optics as well as some practical aspects of the field such as lens design are described in chapter 1. The fundamentals of charged particle optics, such as the paraxial approximation and aberration theory are briefly discussed.

In chapter 2, the historical evolution of electron-beam lithography is described from the early era of focused electron beams to modern electron-optical concepts ever challenging the limits in resolution, pattern complexity, and throughput. A short overview of the possible exposure modes and the patterning process is given as well as some of the other techniques offering sub-micron or nanometer-scale patterning are listed.

In chapter 3, the optical column of the Tesla BS600 series electron-beam writer is described as this machine was chosen as the basis of the aberration correction studies conducted within the scope of this thesis. The changes necessary for converting the shaped-beam column into a Gaussian-beam writer are given and the properties of such a system described.

The goal of this thesis is to study the possibilities of dynamic corrections of field curvature, astigmatism, and distortion in an electron-beam writer. Chapters 4 and 5 are the core of the thesis, they contain the methods used during the writing of the thesis and the results obtained. In chapter 4, the current magnetic beam deflection system and dynamic focusing is studied and complemented with a magnetic stigmator. The optimal excitation of the correction devices is treated, and their ability to eliminate the field curvature and astigmatism aberrations is evaluated.

In chapter 5, a new electrostatic beam deflection system is designed and optimized. Electrostatic dynamic focus lenses and a dynamic stigmator are also added to the model. The optimal properties of these devices are derived and confirmed. The effect of the additional correctors on the distortion is also discussed.

1 CHARGED PARTICLE OPTICS

Charged particle optics is a mathematical framework for the calculation of particle paths in the presence of electrostatic or magnetostatic fields, and for the evaluation of optical properties of electron and ion lenses. The term *optics* is used as a beam of charged particles can be steered by electromagnetic fields in a similar fashion to the manipulation of light rays with lenses in conventional light optics. This framework is essential when designing e.g. scanning or transmission electron microscopes (SEM, TEM), mass and energy filters, and particle accelerators.

The resolution of any imaging microscope is ultimately limited by diffraction and can never be significantly smaller than the wavelength of the image-forming light. This realization comes from Ernst Abbe (1870), who also proposed that there might be a yet undiscovered form of radiation with shorter wavelength than light, that would enable higher resolution imaging. Shortly after, the electron was discovered, and Louis de Broglie postulated in 1924 that it can behave as a wave with very short wavelength when accelerated. The wavelength of an electron with a kinetic energy above 1 keV is smaller than the radius of a hydrogen atom. Diffraction of electrons was first observed by Clinton Davisson and Lester Germer who, with their famous experiment, proved the de Broglie hypothesis and confirmed the wave-like properties of electrons. It didn't take long to utilize the short wavelength of electrons (and ions), and the first electron microscopes became available...

The next sections aim to guide the reader through the most fundamental equations in particle optics following the footsteps of [1] and [2]. For more thorough explanation we refer the reader to e.g. [3] or [4]. This thesis is mainly concerned with electron optics but the same principles apply to ion optics.

1.1 Equation of Motion

The electric field intensity $\vec{E}$ and magnetic flux density $\vec{B}$ acts on charged particles with the Lorentz force

$$\vec{F_L} = q(\vec{E} + \vec{v} \times \vec{B}), \tag{1.1}$$

where q is the charge of the particle, and $\vec{v}$ its velocity. According to Newton's second law the force acting on an object is equal to the change of its momentum

$$\frac{\mathrm{d}\vec{p}}{\mathrm{d}t} = \vec{F_L} \tag{1.2}$$

which, considering that for high-energy electrons relativistic kinematics must be used, can be written as

$$\frac{\mathrm{d}}{\mathrm{d}t}(\gamma m \vec{v}) = q(\vec{E} + \vec{v} \times \vec{B}), \tag{1.3}$$

$$\gamma = \frac{1}{\sqrt{1 - \frac{v^2}{c^2}}} \tag{1.4}$$

where m is the rest mass of the particle and c is the speed of light in vacuum. In particle optics devices, it is advantageous to use an orthogonal coordinate system in which the z axis is usually coincidental with the optical axis along which the particles propagate. We are rarely interested in the solution of the equation of motion (1.3) as a function of time $x = x(t)$, $y = y(t)$, $z = z(t)$. Instead we aim to solve the *trajectory equation* to get $x = x(z)$, $y = y(z)$. For that, let us define the electrostatic potential Φ so that the potential energy is nonnegative and equal to the kinetic energy

$$e\Phi = \gamma mc^2 - mc^2, \tag{1.5}$$

where $e = |q|$. It is common to define the relativistically corrected potential $\Phi^* = \Phi\,(1 + \varepsilon\Phi)$ with a relativistic correction $\varepsilon = e/(2mc^2)$. The Lorentz factor γ in equation (1.4) is then equal to $\gamma = 1 + 2\varepsilon\Phi$.

Assuming that the z-component of the velocity vector $\vec{v}$ is always positive we can write

$$v = \frac{\mathrm{d}z}{\mathrm{d}t}\sqrt{1 + x'^2 + y'^2}, \tag{1.6}$$

$$\frac{\mathrm{d}z}{\mathrm{d}t} = \frac{1}{\gamma}\sqrt{\frac{2e\Phi^*}{m}}\frac{1}{\sqrt{1 + x'^2 + y'^2}}, \tag{1.7}$$

where the primes denote differentiation with respect to the z coordinate. The equation of motion (1.3) can be expressed as the so called *trajectory equation*. In complex notation $w(z) = x(z) + \mathrm{i}y(z)$, $\bar{w}(z) = x(z) - \mathrm{i}y(z)$, it is written as

$$\frac{\mathrm{d}}{\mathrm{d}z}\left(\sqrt{\frac{\Phi^*}{1 + w'\bar{w}'}}\,w'\right) = -\frac{1}{2}\gamma\sqrt{\frac{1 + w'\bar{w}'}{\Phi^*}}\,E_w - \mathrm{i}\eta\left(B_w - w'B_z\right), \tag{1.8}$$

where $w'(z) = x'(z) + \mathrm{i}y'(z)$ is the complex slope of the ray $w(z)$, $\eta = \sqrt{e/(2m)}$, $E_w = E_x + \mathrm{i}E_y$ is the electric field intensity, $B_w = B_x + \mathrm{i}B_y$ is the magnetic flux density in the plane perpendicular to the z axis, and B_z is the z-component of the magnetic field vector.

1.2 Multipole Expansion of the Electromagnetic Field

In charged particle optics, we rarely encounter time-dependent fields, as in most cases, the transition time of the particle through the system is much shorter than the maximum frequency of the field. Hence we can consider the fields stationary. The beam-guiding electric and magnetic fields are formed by the voltages applied to the electrodes and by the currents within the coils of the magnets. These boundary conditions determine the spatial distribution of the fields. In scanning electron-beam applications, the current density of the beam is usually low enough to justify neglecting the space-charge effects (an exception is e.g. electron-beam welding or in the vicinity of electron sources). We assume that only external charges and currents create the electromagnetic field; adding the stationary condition $\partial/\partial t = 0$, the Maxwell equations adopt a simple form

$$\vec{\nabla} \times \vec{E} = 0, \qquad \vec{\nabla} \times \vec{B} = 0, \qquad \varepsilon_0\vec{\nabla}\vec{E} = 0, \qquad \vec{\nabla}\vec{B} = 0, \tag{1.9}$$

where ε_0 is the permittivity of free space. The first two equations are satisfied if the fields are expressed as the gradient of a scalar potential

$$\vec{E} = -\vec{\nabla}\Phi, \qquad \vec{B} = -\vec{\nabla}\Psi. \tag{1.10}$$

Both the electric potential Φ and the scalar magnetic potential Ψ satisfy the Laplace equation

$$\vec{\nabla}^2\Phi = 0, \qquad \vec{\nabla}^2\Psi = 0. \tag{1.11}$$

The potentials on the boundary surfaces (electrodes, pole pieces) determine the solutions of these equations.

In Cartesian coordinates, for systems with a straight axis, the electric potential Φ can be decomposed into a sum of multipole terms

$$\Phi(w, \bar{w}, z) = \sum_{n=1}^{\infty} \Phi_n \cos\Big[n(\varphi - \varphi_{n,0})\Big] \tag{1.12}$$

corresponding to a Fourier series expansion, where n is the multipole component and $\varphi_{n,0}$ its initial orientation; Φ_n is not a function of th polar angle φ. In the vicinity of the optical axis, Φ_n can be expressed as an expansion of the axial potential $\phi_n(z)$

$$\Phi_n = \sum_{k=0}^{\infty} \frac{(-1)^k n!}{k!(n+k)!} \left(\frac{w\bar{w}}{4}\right)^k \Re\left\{\bar{w}^n \frac{\partial^{2k}\phi_n(z)}{\partial z^{2k}}\right\}. \tag{1.13}$$

The first few terms of the rotationally symmetric field Φ_0, the dipole field Φ_1, and the quadrupole filed Φ_2 are as follows:

$$\Phi_0(w, \bar{w}, z) = \phi(z) - \frac{1}{4} w\bar{w}\, \phi''(z) + \frac{1}{64} w^2\bar{w}^2 \phi^{(4)}(z) - \cdots \tag{1.14}$$

$$\Phi_1(w, \bar{w}, z) = -\Re\left\{\bar{w}F_1(z)\right\} + \frac{1}{8} w\bar{w}\, \Re\left\{\bar{w}F_1''(z)\right\} - \cdots \tag{1.15}$$

$$\Phi_2(w, \bar{w}, z) = -\Re\left\{\bar{w}^2 F_2(z)\right\} + \frac{1}{12} w\bar{w}\, \Re\left\{\bar{w}^2 F_2''(z)\right\} - \cdots \tag{1.16}$$

where $F_1(z)$ is the axial dipole field, and $F_2(z)$ is the axial quadrupole field.

From equation (1.10) the electric field is

$$E_x = -\frac{\partial\Phi}{\partial x}, \quad E_y = -\frac{\partial\Phi}{\partial y}, \quad E_z = -\frac{\partial\Phi}{\partial z}, \quad E_w = -2\frac{\partial\Phi}{\partial\bar{w}}. \tag{1.17}$$

An expansion for the magnetic potential can be found analogously

$$\Psi_n = \sum_{k=0}^{\infty} \frac{(-1)^k n!}{k!(n+k)!} \left(\frac{w\bar{w}}{4}\right)^k \Re\left\{\mathrm{i}^n \bar{w}^n \frac{\partial^{2k}\phi_n(z)}{\partial z^{2k}}\right\}. \tag{1.18}$$

The first terms of the rotationally symmetric, the dipole, and the quadrupole magnetic potential are

$$\Psi_0(w, \bar{w}, z) = -\int B(z)\,\mathrm{d}z + \frac{1}{4} w\bar{w}\, B'(z) - \frac{1}{64} w^2\bar{w}^2 B'''(z) + \cdots \tag{1.19}$$

$$\Psi_1(w,\bar{w},z) = \Im\left\{\bar{w}D_1(z)\right\} - \frac{1}{8}w\bar{w}\,\Im\left\{\bar{w}D_1''(z)\right\} + \cdots \tag{1.20}$$

$$\Psi_2(w,\bar{w},z) = \Re\left\{\bar{w}^2 D_2(z)\right\} - \frac{1}{12}w\bar{w}\,\Re\left\{\bar{w}^2 D_2''(z)\right\} + \cdots \tag{1.21}$$

where $B(z)$ is the rotationally symmetric axial magnetic flux density, $D_1(z)$ is the axial dipole field, and $D_2(z)$ is the axial quadrupole field.

From equation (1.10) the magnetic field is

$$B_x = -\frac{\partial\Psi}{\partial x}, \quad B_y = -\frac{\partial\Psi}{\partial y}, \quad B_z = -\frac{\partial\Psi}{\partial z}, \quad B_w = -2\frac{\partial\Psi}{\partial\bar{w}} \tag{1.22}$$

1.3 The Paraxial Equation

Substituting the linear terms of the field expansions (1.14)–(1.16) and (1.19)–(1.21) into the trajectory equation (1.8) yields the *paraxial equation*

$$\begin{aligned}\phi^{*1/2}w'' + \left(\frac{\gamma\phi'}{2\phi^{*1/2}} - \mathrm{i}\eta B\right)w' + \left(\frac{\gamma\phi''}{4\phi^{*1/2}} - \frac{\mathrm{i}\eta}{2}B'\right)w +\\ + \left(\frac{\gamma F_2}{\phi^{*1/2}} + 2\eta D_2\right)\bar{w} = \frac{\gamma U_1 F_1}{2\phi^{*1/2}} + \eta I_1 D_1\end{aligned} \tag{1.23}$$

where F_1 and D_1 are weak normalized dipole fields generated by a unit voltage and unit current applied to the electrodes and pole pieces of the deflection system. The dipole fields are then equal to U_1F_1 and I_1D_1, where $U_1 = U_{1x} + \mathrm{i}U_{1y}$ and $I_1 = I_{1x} + \mathrm{i}I_{1y}$ are the applied voltage and current.

1.3.1 Round Lenses and Deflection Fields

In systems with only rotationally symmetric and dipole fields (round lenses and deflectors) the paraxial equation takes the form

$$w'' + \left(\frac{\gamma\phi'}{2\phi^*} - \mathrm{i}kB\right)w' + \left(\frac{\gamma\phi''}{4\phi^*} - \frac{\mathrm{i}k}{2}B'\right)w = \frac{\gamma U_1 F_1}{2\phi^*} + kI_1D_1, \tag{1.24}$$

where $k = \eta/\phi^{*1/2}$. The homogeneous paraxial equation (equation (1.24) with its right-hand side equal to zero, i.e. no dipole fields present) is usually solved for two independent rays: the *axial ray* w_a and the *field ray* w_b with initial values in the *object plane* $z = z_o$

$$w_a(z_o) = 0, \quad w_a'(z_o) = 1, \qquad w_b(z_o) = 1, \quad w_b'(z_o) = 0^2. \tag{1.25}$$

The particular solutions of the inhomogeneous equation are then found by variating the parameters of the homogeneous solution. These can be expressed as

$$w_e(z) = -\frac{1}{2\phi^{*1/2}(z_o)}\left[w_a(z)\int_{z_o}^{z}\frac{\gamma F_1}{\phi^{*1/2}}\bar{w}_b\,\mathrm{d}\zeta - w_b(z)\int_{z_o}^{z}\frac{\gamma F_1}{\phi^{*1/2}}\bar{w}_a\,\mathrm{d}\zeta\right], \text{ and} \tag{1.26}$$

[2] The initial value $w_b'(z_o) = 0$ holds if no magnetic field is present at the object plane $B(z_o) = 0$; in the general case $w_b'(z_o) = \dfrac{\mathrm{i}\eta B(z_o)}{2\phi^{*1/2}(z_o)}$.

$$w_m(z) = \frac{1}{\phi^{*1/2}(z_o)} \left[w_a(z)\,\eta \int_{z_o}^{z} D_1 \bar{w}_b \,\mathrm{d}\zeta - w_b(z)\,\eta \int_{z_o}^{z} D_1 \bar{w}_a \,\mathrm{d}\zeta \right] \tag{1.27}$$

for electrostatic and magnetic dipole fields, respectively [2].

The general solution of the paraxial equation (1.24) can be written as

$$w_p(z) = \alpha_o w_a(z) + \beta_o w_b(z) + I_1 w_m(z) + U_1 w_e(z), \tag{1.28}$$

where $\alpha_o = w'(z_o)$ is the complex ray slope in the object plane, and $\beta_o = w(z_o)$ is the transverse coordinate of the ray in the object plane. The *image plane* $z = z_i$ is located where the axial ray crosses the optical axis $w_a(z_i) = 0$. The magnification of the system M is defined by the field ray in the image $w_b(z_i) = M \exp(\mathrm{i}\theta)$, and the angular magnification by the axial ray $w'_a(z_i) = M_a \exp(\mathrm{i}\theta)$, where θ is the rotation of the meridional plane. The general ray (1.28) can be equivalently given by the ray properties in the image plane

$$w_p(z) = \alpha_i \frac{w_a(z)}{w'_a(z_i)} + \beta_i \frac{w_b(z)}{w_b(z_i)} + \gamma_i \frac{w_m(z)}{w_m(z_i)} + \delta_i \frac{w_e(z)}{w_e(z_i)}, \tag{1.29}$$

where α_i is the ray slope in the image plane, β_i is the size of the image;

$$\begin{aligned} \gamma_i &= I_1 w_m(z_i), \text{ and} \\ \delta_i &= U_1 w_e(z_i) \end{aligned} \tag{1.30}$$

are the image plane coordinates of the ray deflected by magnetic and electrostatic deflectors, respectively.

1.3.2 Electrostatic Lens

In case of solely electrostatic round lenses, the paraxial equation (1.24) contains no imaginary terms; it is equivalent in both directions x and y, and takes the form

$$r'' + \frac{\gamma\phi'}{2\phi^*} r' + \frac{\gamma\phi''}{4\phi^*} r = 0 \tag{1.31}$$

for $r = \sqrt{w\bar{w}}$. By applying the transformation $r(z) = R(z)\left[\phi^*(z_o)/\phi^*(z)\right]^{1/4}$, equation (1.31) takes an even simpler form [2]

$$R'' + \frac{(2+\gamma^2)\,\phi'^2}{16\phi^{*2}} R = 0. \tag{1.32}$$

The propagating rays are confined to the meridional plane as there are no lateral forces acting on them in a purely electrostatic lens configuration. A single real coordinate $R(z)$ is sufficient to define the ray.

1.3.3 Magnetic Lens

Assuming only round magnetic lenses, the paraxial equation (1.24) is written as

$$w'' - \mathrm{i}kBw' - \frac{\mathrm{i}k}{2} B' w = 0. \tag{1.33}$$

Writing the complex $w(z)$ in polar form $w(z) = r(z)\exp[\mathrm{i}\theta(z)]$, we obtain two real equations [2]

$$r'' + \frac{k^2 B^2}{r} = 0, \qquad \theta' = \frac{k}{2}B. \tag{1.34}$$

Rays in magnetic lenses undergo Larmor precession, i.e. the meridional plane rotates as the ray propagates in the magnetic field by the angle

$$\theta(z) = \frac{k}{2}\int_{z_o}^{z} B(\zeta)\,\mathrm{d}\zeta \tag{1.35}$$

creating a rotating coordinate system where the ray is defined by its polar coordinate r.

1.3.4 Paraxial Properties of Lenses

As the result of neglecting higher order terms in the trajectory equation, the paraxial equation describes the propagation of particles accurately only in a limited volume close to the optical axis. Rays further from the optical axis deviate from this ideal solution. The paraxial or Gaussian approximation was introduced by C. F. Gauss in light optics. Paraxial behavior enables one to describe the optical properties of various elements in a simple way by characteristic quantities such as focal length and principal planes. These can be derived from the paraxial equations (1.32) and (1.34).

1.4 Aberrations

The deviation of real rays from the paraxial approximation can be expressed with additional terms $P(z)$ on the right-hand side of the paraxial equation (1.24). As opposed to taking the linear terms only as in the paraxial approximation, higher order terms of w and w' in the field expansion are included; we will consider terms up to the third order $P_3(z)$. As not all particles have the same energy, it is advantageous to include another term, $P_c(z)$, which is proportional to the particle energy deviation $\Delta\phi$. With this term included, one can characterize the energy distribution as an aberration of the paraxial optics. The equation containing these aberrations takes the form

$$w'' + \left(\frac{\gamma\phi'}{2\phi^*} - \mathrm{i}kB\right)w' + \left(\frac{\gamma\phi''}{4\phi^*} - \frac{\mathrm{i}k}{2}B'\right)w = \frac{\gamma U_1 F_1}{2\phi^*} + kI_1 D_1 + P_3(z) + P_c(z). \tag{1.36}$$

Analogously to the paraxial equation with added dipole fields, one solves equation (1.36) with the variation of parameters method. The general solution is given by

$$w(z) = w_p(z) + \Delta w(z), \tag{1.37}$$

where $w_p(z)$ is the paraxial solution (1.29), and $\Delta w(z)$ is the deviation of the trajectory introduced by the additional terms $P(z)$.

1.4.1 Third-order Geometric Aberrations

Let us consider the aberrations introduced by $P_3(z)$ in equation (1.36). These are the so called third-order geometric aberrations and are the result of including the third-order terms of w of the field expansions in the trajectory equation. Analogously to light optics, the aberrations of round lenses are: spherical aberration k_S, astigmatism k_A, coma k_L, field curvature k_F, and distortion k_D. In case of magnetic lenses, the aberrations k_A, k_L, and k_D are complex. The deviation of the real ray from the paraxial trajectory in the image plane due to the geometric aberrations is given by

$$\Delta w(z_i) = k_S\alpha_i^2\bar{\alpha}_i + k_A\bar{\alpha}_i\beta_i^2 + k_L\alpha_i\bar{\alpha}_i\beta_i + \frac{1}{2}\bar{k}_L\alpha_i^2\bar{\beta}_i + k_F\alpha_i\beta_i\bar{\beta}_i + k_D\beta_i^2\bar{\beta}_i \tag{1.38}$$

expressing the aberration coefficients and ray parameters in the image plane [5].

For dipole deflection fields with equivalent x and y direction deflection, and with no hexapole field component, the structure of aberration coefficients takes a similar form as in the case of round lenses

$$\begin{aligned}\Delta w(z_i) = {} & K_A^m\bar{\alpha}_i\gamma_i^2 + K_L^m\alpha_i\bar{\alpha}_i\gamma_i + \frac{1}{2}\bar{k}_L^m\alpha_i^2\bar{\gamma}_i + K_F^m\alpha_i\gamma_i\bar{\gamma}_i + K_D^m\gamma_i^2\bar{\gamma}_i + \\ & + K_A^e\bar{\alpha}_i\delta_i^2 + K_L^e\alpha_i\bar{\alpha}_i\delta_i + \frac{1}{2}\bar{k}_L^m\alpha_i^2\bar{\delta}_i + K_F^e\alpha_i\delta_i\bar{\delta}_i + K_D^e\delta_i^2\bar{\delta}_i + \\ & + S_A\bar{\alpha}_i\gamma_i\delta_i + S_F\alpha_i\bar{\gamma}_i\delta_i + \bar{S}_F\alpha_i\gamma_i\bar{\delta}_i + K_D^m\gamma_i^2\bar{\gamma}_i + \\ & + S_{D1}\bar{\gamma}_i\delta_i^2 + S_{D2}\gamma_i\delta_i\bar{\delta}_i + S_{D3}\gamma_i\bar{\gamma}_i\delta_i + S_{D4}\gamma_i^2\bar{\delta}_i + \\ & + \varsigma_{D1}\beta_i\bar{\gamma}_i\delta_i + \varsigma_{D2}\bar{\beta}_i\gamma_i\delta_i + \varsigma_{D3}\beta_i\gamma_i\bar{\delta}_i,\end{aligned} \tag{1.39}$$

where the deflections γ_i and δ_i are defined by equation (1.30), the coefficients K^m are the aberrations of the magnetic deflection, K^e are those of the electrostatic deflection, S are mixed aberrations of combined deflection systems, and ς are aberrations related to the finite size of the object [5]. In reality, using a single deflection system and imaging with a narrow beam, only a single type of aberrations, e.g. K^m, is nonzero. The image position deviation can be expressed, analogously to the case of round lenses, using the ray parameters in the object plane with the definitions $\gamma_i = M\exp(\mathrm{i}\theta)\gamma_o$ and $\delta_i = M\exp(\mathrm{i}\theta)\delta_o$.

Although not being a third-order aberration, it is important to note the effect of defocus on the image position as this is often used to lower the impact of the mentioned aberrations. In the observation plane z_{obs} in a small distance $\Delta z = z_{\mathrm{obs}} - z_i$ from the Gaussian plane (paraxial image plane) z_i the ray position is given by

$$w(z_{\mathrm{obs}}) = w(z_i) + \Delta z\left(\alpha_i + \gamma_i' + \delta_i' + \frac{\beta_i}{f_i}\right), \tag{1.40}$$

where γ_i' and δ_i' are the slopes of the deflected trajectories in the image plane, and f_i is the focal length of the lens [5].

Spherical Aberration

The spherical aberration is the only aberration that does have an effect even if the object is situated at the optical axis. If the beam is limited by a circular aperture, the spherical aberration broadens the Gaussian image point into a disk with radius $r_s = k_S \alpha_{i,\max}^3$, where $\alpha_{i,\max}$ is the maximum aperture angle in the image plane. The spherical aberration is the result of the lens's focusing power increasing with off-axis distance. The index of refraction is related to the field potential which must satisfy the Laplace equation. Since the charges and currents generating the field are far from the axis, the potential Φ must inherently increase with radial distance [3]. This leads to an always positive spherical aberration for both electrostatic and magnetic lenses as proved by Scherzer in 1936[2] [6]. Rays passing through the lens further from the axis are therefore always focused more strongly than paraxial rays as shown in figure 1.1. One finds that placing the detecting plane closer to the lens (negative defocus) the spot size is considerably smaller down to the *disk of least confusion*.

Astigmatism and Field Curvature

Astigmatism and field curvature are closely associated aberrations. These aberrations arise when imaging off-axis objects with incident rays striking the optical system at an angle. Astigmatism is the phenomenon where a lens has different focusing power in the x and y directions. Two line images are formed at different image surfaces as shown in figure 1.2. The spot at the Gaussian image plane is elliptical. It is possible to find an ideal surface between the astigmatic images where the image of a point object is a disk of minimal size. This ideal surface is curved, hence the name of the aberration — field curvature. The field curvature of round electron lenses is, as in the case of spherical aberration, always positive.

The field curvature of deflection systems can be compensated dynamically by lowering the focusing power of the lens proportionally to the square of the deflection

[2]Scherzer's theorem holds for rotationally symmetric, static, space-charge-free, dioptric lenses. By abandoning one or more of these criteria, it is possible to design lenses with negative spherical aberration.

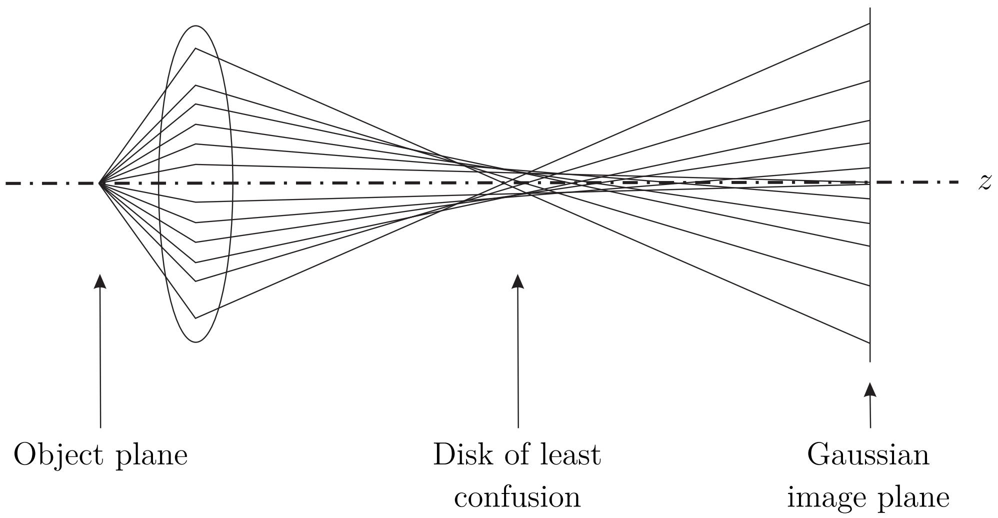

Figure 1.1: Positive spherical aberration of an electron lens. Rays further from the axis are focused more strongly than paraxial rays. The resulting image of a point object is a finite disk. According to [3].

$\gamma_i\bar{\gamma}_i$. The deflection astigmatism can be corrected by introducing a quadrupole field (stigmator) proportional to γ_i^2. The dynamic correction of these aberrations is the main goal of this thesis and will be discussed in chapters 4 and 5.

Coma

Coma results in off-axis point objects appearing to have a tail like a comet. Coma is defined as a variation of magnification over the entrance pupil. Coma is characterized by linear shift of the image (coma length k_L) and the broadening of the image of a point into a disk (coma radius $\bar{k}_L/2$). These two effects occur simultaneously creating the characteristic comet-like shape as shown in figure 1.3.

Distortion

All previously discussed aberrations depend on the aperture radius. If the aperture is small enough so that the system does not exhibit these aberrations, one aberration still remains — distortion. In Gaussian optics, the magnification is constant

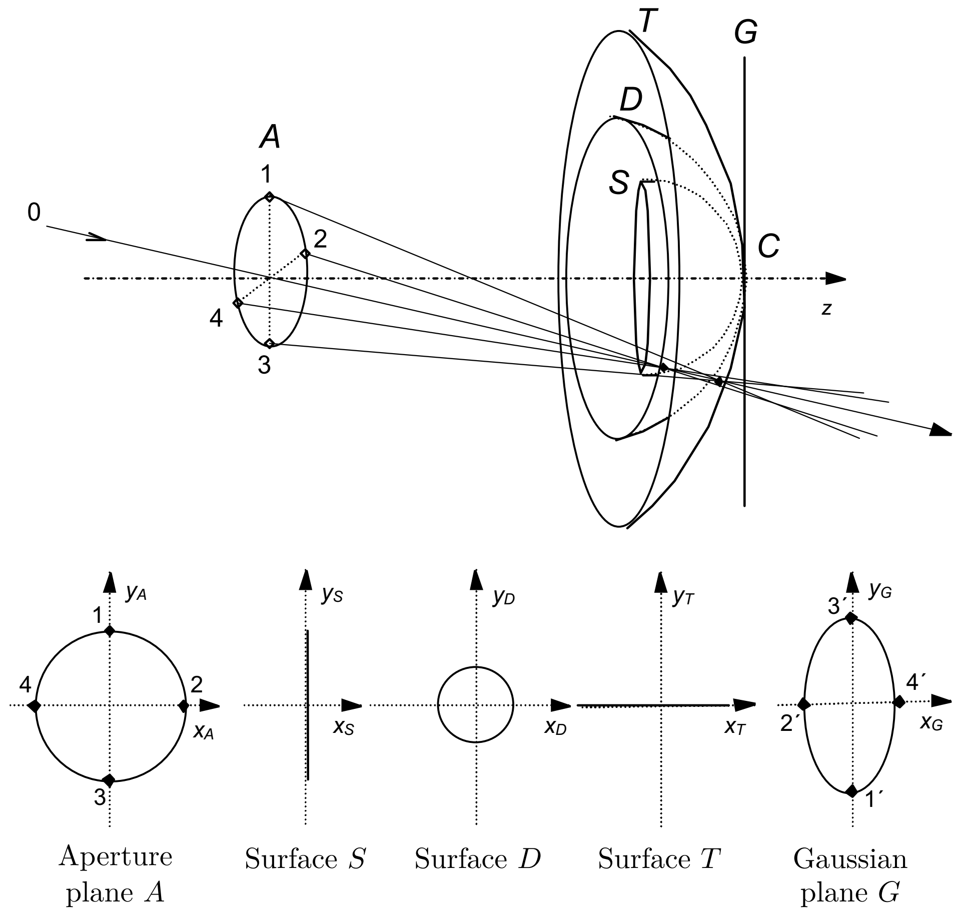

Figure 1.2: The effect of astigmatism and field curvature. Astigmatism forms two line images of a point object at different image surfaces S and T. Field curvature causes that the optimal surface D between the two astigmatic images is curved. From [1].

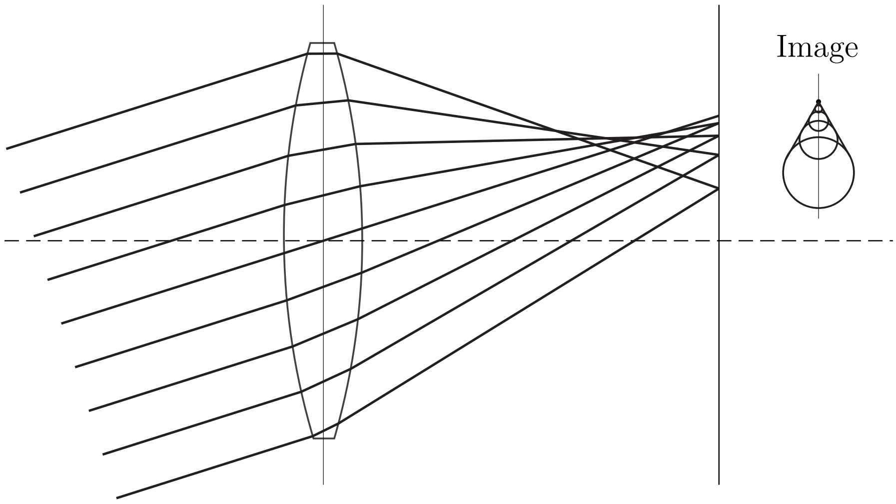

Figure 1.3: Coma results in an off-axis point object appearing to have a tail like a comet. Coma is defined as a variation of magnification over the entrance pupil. According to [7].

regardless of the object size. In real systems, however, the magnification is a function of off-axial distance of the ray. Two possibilities arise: in *barrel distortion* the magnification decreases with distance from the optical axis, whereas in *pincushion distortion* the magnification increases. The names of these aberrations are evident from the shape of the image of a rectangular grid as can be seen in figure 1.4. The nature of distortion depends on the position of the aperture.

The distortion of deflection systems shifts the image of the axial point object in the image plane. This can be compensated by superimposing a small correction onto the deflection signal. The compensation of deflection distortion will be addressed in chapter 5.

1.4.2 Chromatic Aberrations

Chromatic aberrations are a consequence of the finite energy distribution of beam electrons. The index of refraction is a function of the electron energy. Electrons with different initial energy will therefore follow different trajectories, and the image of a point object becomes a disk with finite dimensions. The chromatic aberration of an electron lens is shown if figure 1.5. Compared to light optics, the energy distribution of electrons $\Delta\Phi/\Phi$ in charged particle applications is relatively narrow, typically around $10^{-6} - 10^{-4}$. Chromatic aberrations are divided into *axial chromatic aberration* and *chromatic distortion*. As in the case of the spherical aberration, the axial chromatic aberration cannot be eliminated by skillful design.

The ray position deviation in the image plane due to first-order chromatic aberrations is given by

$$\Delta w(z_i) = (k_x\alpha_i + k_T\beta_i + K_T^m\gamma_i + K_T^e\delta_i)\,\frac{\Delta\Phi}{\Phi^*}, \tag{1.41}$$

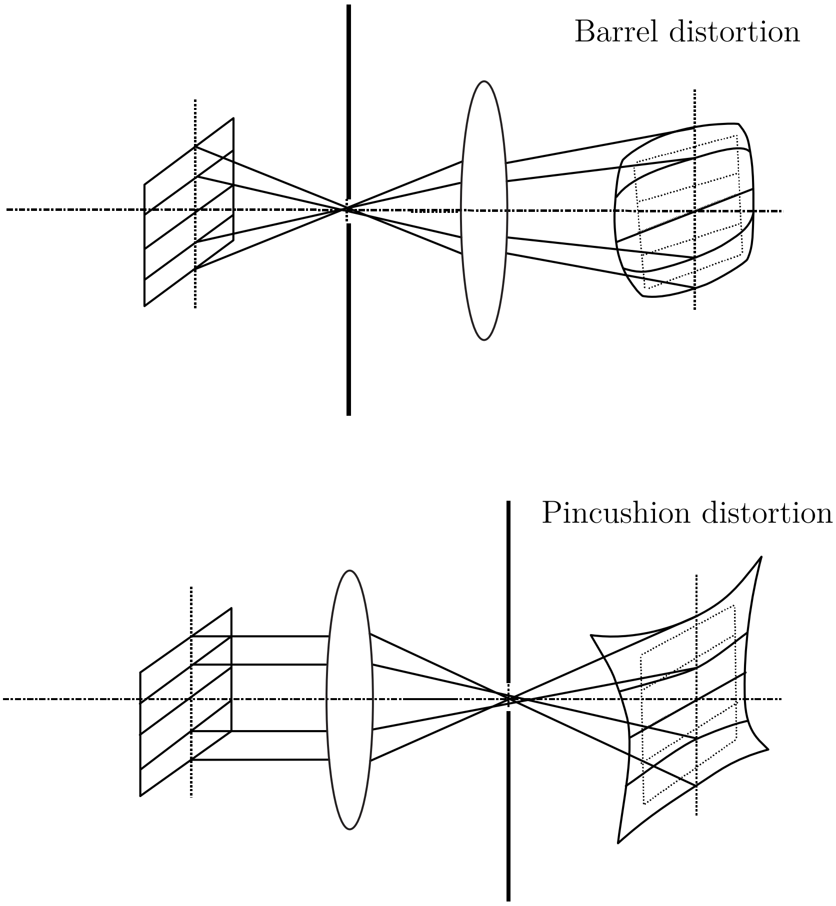

Figure 1.4: Distortion of the image of a rectangular grid. The magnification of the system is a decreasing or increasing function of off-axial distance of the ray resulting in barrel- or pincushion distortion, respectively. The nature of distortion depends on the position of the aperture. According to [1].

where k_{xi} is the axial chromatic aberration of round lenses, k_{Ti} is the chromatic distortion of round lenses, and K_{Ti} is the deflection chromatic aberration; all aberration coefficients and ray parameters are given with respect to the image plane z_i.

The chromatic aberrations can be lowered by employing a monochromator which filters the energy distribution of the electrons. The disadvantage of this solution is that it decreases the beam current. Another method of compensating chromatic aberrations is to introduce multipole fields which can have negative chromatic aberration.

1.4.3 Other Aberrations

Several other aberrations affect the performance of an electron-beam device. These will not be considered in this thesis as they are negligibly small in our studies; however we give a short description of the most important ones.

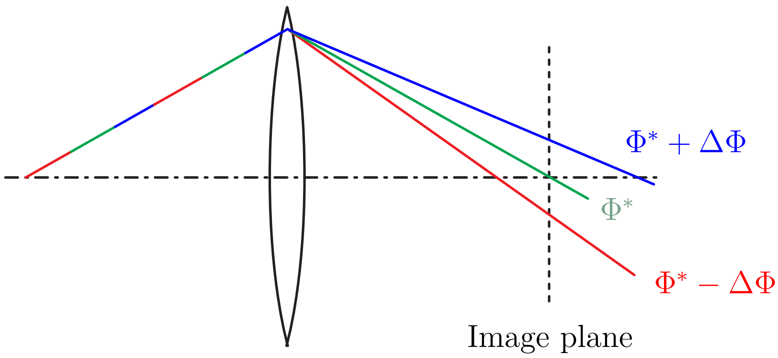

Figure 1.5: Axial chromatic aberration of an electron lens. Electrons with higher energy are focused less strongly than electrons with lower energies. As a consequence, the image of a point object is a finite-size disk. According to [3].

Space Charge

Beam particles interact with each other via their electromagnetic field. In case of an electron beam the electrostatic repulsion between electrons causes broadening of the beam. This is most noticeable in regions with high current density and low particle energy. In most scanning electron-beam applications the effect of space charge is negligible; it needs to be taken into consideration in the vicinity of electron sources, however.

Diffraction

Diffraction is the result of the wave-like nature of electrons. Electrons diffract on apertures causing image blur; here the principles of geometrical optics can no longer be applied. According to the de Broglie theorem, particles with momentum p have a wavelength

$$\lambda = \frac{h}{p}, \tag{1.42}$$

where $h = 6.63 \times 10^{-34}$ Js is the Planck constant. Imaging with electrons of wavelength λ creates a diffraction pattern in the image plane characterized by the Airy function. The highest intensity disk at the center of the Airy pattern has a diameter

$$d = 1.22\frac{\lambda}{\alpha}, \tag{1.43}$$

where α is the aperture angle. To limit the effects of diffraction in charged particle optics, greater aperture angles are preferred, whereas e.g. the spherical aberration is proportional to the (cube of the) aperture angle. An optimal aperture angle can be found in all applications after evaluating all contributing aberrations.

Parasitic Aberrations

In practice, imperfections in construction and misalignment of electron-optical elements will always disturb the ideal shape and symmetry. These effects generate additional aberrations known as *parasitic aberrations*. The perturbation of the ideal system by the imperfections is small, and therefore can be treated using perturbation theory. The most known parasitic aberration is the axial astigmatism which is caused by the ellipticity of lenses generating a weak quadrupole field. This is routinely canceled in electron microscopes by introducing a stigmator which produces its own quadrupole field [8].

1.5 Optical Elements

1.5.1 Electron Gun

The electron gun incorporates the emitter (cathode) and the acceleration stage. Particles are emitted from very small thermionic, Schottky, or field-emission cathodes; they are then accelerated and focused by a strong electrostatic field to energies on the order of 10–100 keV in electron microscopy applications. From an electron-beam system design point of view, the most important parameters of the gun are: 1) *brightness* β, defined as the current passing through unit area into a solid (aperture) angle; and 2) the initial *energy spread* ΔE of the electrons.

In thermionic emission, electrons from the Fermi level of the cathode can overcome the work function by thermionic excitation. These cathodes operate at 1400–2000 K depending on their material [9]. Most commonly W or LaB_6 cathodes are used. Thermionic emission guns offer a brightness around 10^{10} [$Am^{-2}sr^{-1}$] and the beam energy spread is 1.5 eV [10].

In a Schottky-type emitter, the work function is decreased by a strong electric field at the tip of the cathode. The work function us usually further lowered by coating the tip. Schottky cathodes are operated at temperatures around 1800 K. The brightness of Schottky emitters is $5{\times}10^{12}$ [$Am^{-2}sr^{-1}$], and their energy spread is 0.3–1 eV [10].

Field emission occurs when the electrical field around the cathode tip decreases the width of the potential barrier to a few nanometers. The electrons from the Fermi level can penetrate this barrier by the tunneling effect. Field emission guns require ultra-high vacuum, otherwise the tip is rapidly destroyed by residual atmosphere ion bombardment. Field emission guns can operate at room temperature but often work at 1000–1500 K to avoid adsorption. The lower cathode temperature results in lower energy spread $\Delta E \approx 0.3$ eV. The brightness of field emission guns is 10^{11}–10^{13} [$Am^{-2}sr^{-1}$].

For further information on electron guns we refer the reader to [9]. A thorough characterization of electron guns was performed by Horak in his bachelor's thesis [10].

1.5.2 Round Lenses

Round lenses generate a rotationally symmetric electrostatic or magnetic field which focuses the electron beam. These lenses have cylindrical bores and are precisely arranged on a common axis.

Electrostatic lenses

Electrostatic lenses consist of several charged electrodes which produce the focusing field. They can be divided by the number of electrodes they use according to [11].

Aperture The simplest electrostatic lens with a focusing effect is an aperture dividing two regions with different electrostatic potential. The aperture acts as a converging lens for electrons entering the region with higher potential, and as a diverging lens for electrons entering the lower potential region.

Immersion lens An electrostatic immersion lens can be created by two cylindrical electrodes with different potential. Much like in the aperture lens case, the immersion lens can be converging or diverging.

Unipotential lens The most commonly used electrostatic lens is the unipotential or *einzel* lens. The lens consists of three circular or cylindrical electrodes. In symmetric unipotential lenses, the shape and the applied potential to the outer electrodes is equal. The object and image region are on the same potential in this case, and the focusing power of the lens is adjusted by the potential applied to the center electrode — hence the name. Unipotential lenses are always converging, and can be operated in *accelerating* or *decelerating* mode defined by the potential of the central electrode relative to the outer electrodes. The focusing effect of the unipotential lens can be seen in figure 1.6, from which it is evident that an accelerating lens has lower aberrations. In practice, however, decelerating mode is commonly preferred for finer tuning and to avoid breakdown discharges between electrodes.

Zoom lenses Zoom lenses use four or more electrodes to achieve adjustable magnification for a given object and image position.

For a more detailed description of electron lenses, their use and properties we refer the reader to [11].

Magnetic lenses

As in case of electrostatic fields, an axially symmetric magnetic field has a focusing effect on charged particles. Magnetic lenses offer higher focusing power and lower aberrations than their electrostatic counterparts for electron energies used in electron microscopy. Another important note is that charged particles undergo Larmor precession in an axial magnetic field, thus the beam rotates in a magnetic lens. In order to maximize the focusing effect, the coil is surrounded by a magnetic casing allowing the field to reach the optical axis only via a small region — gap — between carefully designed pole pieces. A simple design of a magnetic objective lens is shown in figure 1.7. For a detailed treatment of magnetic lens design, we refer to the reader to [12] or [13].

1.5.3 Deflectors

Deflectors produce a dipole field to deflect the particle beam off-axis. Electrostatic or magnetic dipole fields can be both used, while magnetic deflectors offer stronger deflection force and lower aberrations in general. If potential of the deflector is antisymmetrical around the optical axis in the x and symmetrical in the perpendicular y

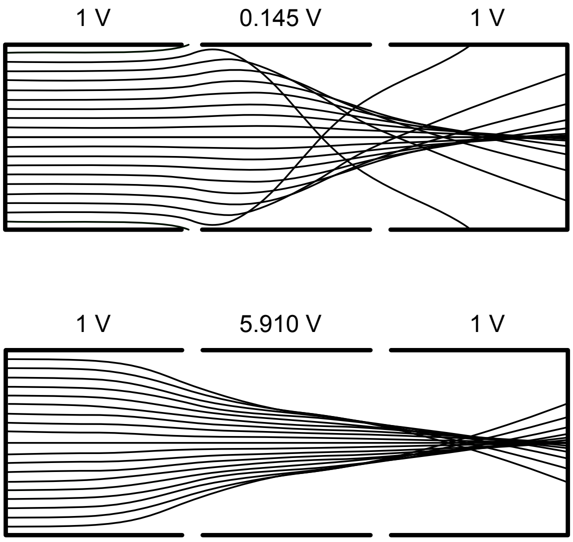

Figure 1.6: Electrode arrangement of a unipotential electrostatic lens. The ray traces show that the lens is converging in decelerating and accelerating voltage modes. The Gaussian image of the entering parallel beam is in the right-hand electrode plane; rays being focused more strongly is the result of spherical aberration which is noticeably higher in the decelerating mode. From [11].

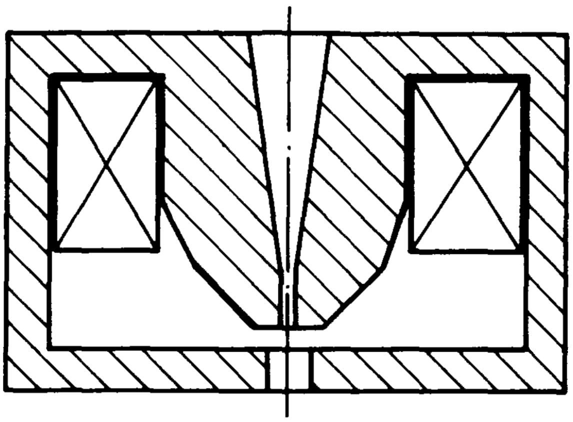

Figure 1.7: A simple design of a magnetic objective lens around the optical axis depicting the coil (crosshatch) inside the casing (section lines). The gap is formed by the pole pieces in the opening of the casing. From [12].

direction, the quadrupole and octupole field components vanish, leaving the hexapole field the first non-zero multipole [14]. Important aspects of deflector design are high homogeneity of the dipole field around the optical axis (at least up to the deflected beam off-axis distance), and that they do not produce a hexapole field.

Electrostatic deflectors in charged particle microscopy are made of cylindrical electrodes. While satisfying the equivalent x and y direction deflection condition, equisectored 8-electrode deflectors or non-equisectored 20-electrode deflectors can be used; these are shown schematically in figure 1.8. With appropriate choice of voltage on the electrodes, the hexapole field component vanishes. For this, the 8-electrode systems needs two voltage supplies, while only one is sufficient for the 20-electrode system. However, twenty electrodes pose a considerable challenge in the manufacturing process.

Magnetic deflectors can be made of toroidal or saddle coils as shown in figure 1.9. A high frequency magnetic deflector induces eddy currents in nearby conductors, such as lens casing, pole pieces, etc., greatly limiting its performance. This can be compensated by enclosing the deflector in another set of deflection coils with opposite excitation which partially cancel the outer magnetic field [14]. Appropriate design of coil geometry allows nullifying the hexapole field.

1.5.4 Stigmators

Stigmators produce a quadrupole field and are used mainly to compensate the axial astigmatism. They can also be used to compensate deflection astigmatism, as will be discussed in chapters 4 and 5. As in case of deflectors, stigmators can be electrostatic or magnetic. In fact, it is possible to produce an independent quadrupole field using an 8-electrode deflection system. Figure 1.10 shows how a quadrupole field of arbitrary orientation can be produced using an 8-electrode stigmator. Figure 1.11 shows the creation of an arbitrarily oriented quadrupole using saddle coils.

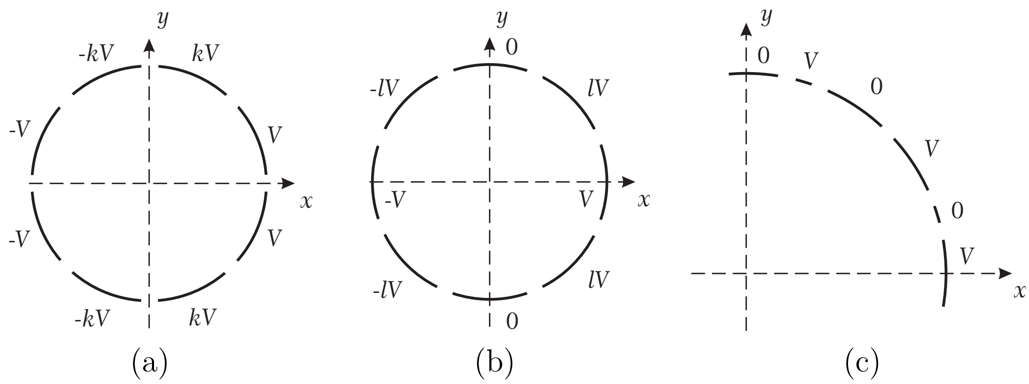

Figure 1.8: Electrodes of two 8-electrode equisectored deflector (a) and (b), and a non-equisectored 20-electrode deflector (c) deflecting in the x direction. For $k = \sqrt{2} - 1$ and $l = \sqrt{2}/2$, as well as in (c), the hexapole field vanishes. From [14].

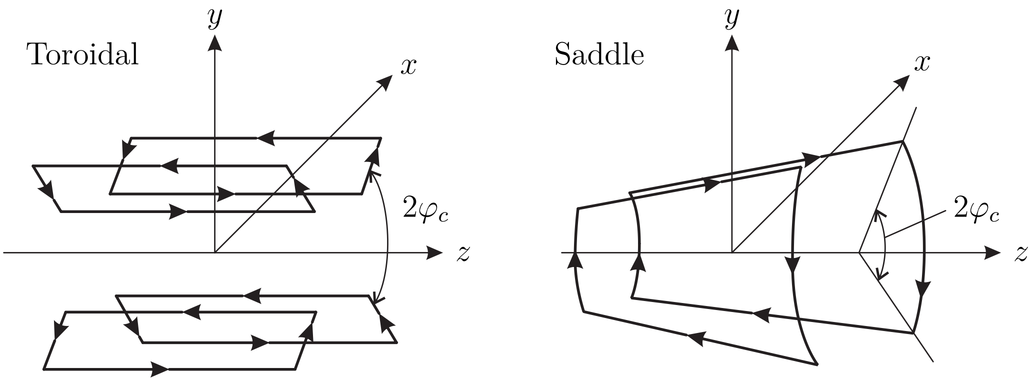

Figure 1.9: Toroidal and tapered saddle magnetic deflector coils deflecting in the x direction. The hexapole field component vanishes for $2\varphi_c = 60°$. According to [15].

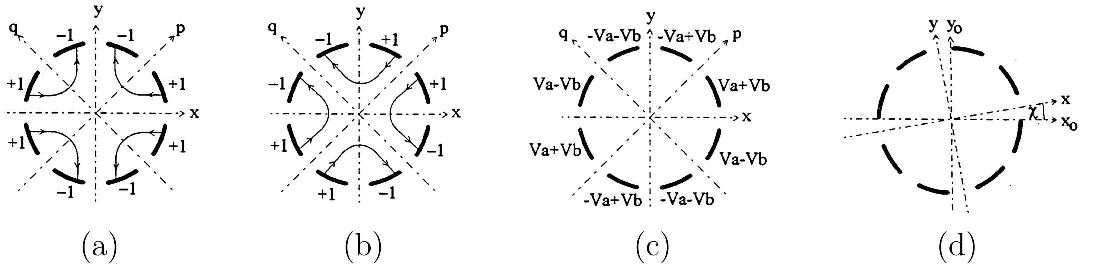

Figure 1.10: An electrostatic 8-electrode stigmator. The unit voltages applied to the electrodes of stigmator (a) create a quadrupole field with (x, y) axes. A 45°-rotated quadrupole field with (p, q) axes is created by applying the unit potentials shown in (b). A quadrupole field of arbitrary orientation (c) can be created as a linear combination of (a) and (b). Alternatively the stigmator may be physically rotated by an angle χ. From [16].

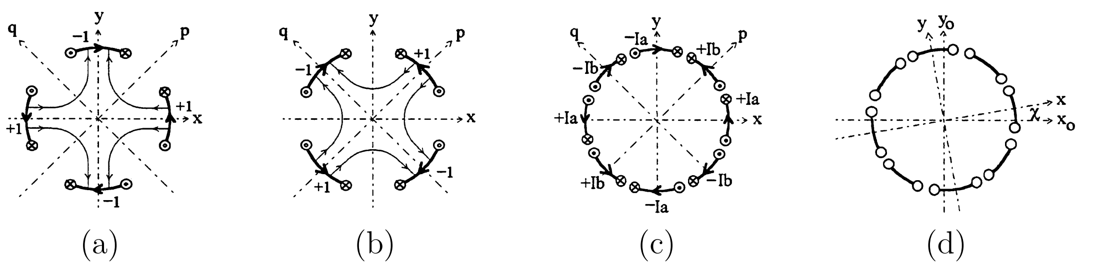

Figure 1.11: A magnetic saddle-coil stigmator. The unit current in the saddle coils (a) produces a quadrupole field with (x, y) axes. A 45°-rotated quadrupole field with (p, q) axes is created by applying the unit current shown in (b). A quadrupole field of arbitrary orientation (c) can be created as a linear combination of (a) and (b). Alternatively the stigmator may be physically rotated by an angle χ. From [16].

1.6 Computer-aided Design

To design an electron-optical system, it is essential to be able to predict its attributes: the paraxial properties and the aberration coefficients. A fast method is needed to evaluate the effect of the shape and position of the optical elements on the performance of the system. The amount of calculations involved makes it necessary to use computer tools in modern charged particle optics applications. Software for the design of electron microscopes and lithography systems has become commercially available. In principle, two options are available: 1) ray tracing and 2) solving the paraxial equation and evaluating the aberration coefficients. In microscopy, aberrations theory is used to a great extent as it provides a set of coefficients to characterize and compare optical elements and systems.

In this thesis, EOD (Electron Optical Design [17]) is used for the design and evaluation of the electron-beam lithography system properties. The software package offers a design environment, field calculation using the finite element method, ray tracing, and evaluation of paraxial properties and aberrations.

2 DIRECT-WRITE ELECTRON-BEAM LITHOGRAPHY

Electron-beam lithography (EBL) is a technique for creating extremely fine patterns using a focused electron beam. The term “direct-write” refers to the beam scanning across the surface drawing custom shapes as opposed to mask-writing. The surface is coated with an electron-sensitive layer called a resist which changes its structure when exposed to the beam of electrons. Patterns of sub-10 nm resolution can be created this way making EBL a requirement for modern electronics and integrated circuit fabrication. The main features of direct-write electron-beam lithography are

1. High resolution, almost to the atomic level. A feature size of 2 nm and 8 nm half-pitch (half the distance between identical features) has been reported by Manfrinato et al. [18].
2. High flexibility. There are almost no restrictions for the pattern to be generated as it is a maskless technique, and EBL is compatible with a great variety of materials.
3. Low speed. Compared to projection techniques, direct-write EBL is one or more orders of magnitude slower.
4. High price. Commercially available EBL machines are very costly with price tags ranging up to several million dollars.

2.1 Evolution of Electron-Beam Lithography

Writing miniature features with an electron beam was proposed in 1959 by Richard Feynman in his famous address to the American Physical Society titled “There’s Plenty of Room at the Bottom” [19]. Feynman suggested using a setup similar to the scanning electron microscope to *“write the entire 24 volumes of the Encyclopedia Britannica on a head of a pin”* [20]. Feynman also foresaw — since the direct modification of metal surfaces with an electron beam would be inefficient — the subsequent discovery of the electron beam resist.

Research along these lines started soon after. In the early 60s electron beams were used to deposit hydrocarbon and silicone from gas phase. Creating high resolution metal lines was demonstrated in the mid 60s using a scanning electron beam with a mask and a photodetector. This method allowed fabrication of 60–80 nm wide aluminum lines [21].

In 1966, IBM researchers demonstrated a lithography tool similar to today’s systems. It consisted of an electron column, a motorized x-y stage, a digital deflection with pattern data stored on magnetic tape, and secondary electron imaging. The instrument could expose photoresists on e.g. silicon wafers. Another group at IBM created a bipolar transistor working at 2 GHz using EBL [22].

Within a few years, the common polymer polymethylmethacrylate (PMMA) was discovered to have optimal properties as a high resolution electron sensitive resist [23]. This was a huge step forward in EBL as previously used photoresists produced much worse results. PMMA allowed the use of a new technique — *lift-off*. It is remarkable, that despite the plethora of technological advancements in electron-beam lithography, PMMA is still widely used as resist nowadays. When exposed to the electron beam, the large molecules of PMMA (10 000–1 100 000 molecular weight) are broken into smaller pieces. These can then be selectively washed away in a solvent developer creating the needed pattern.

In the 1970s, electron-beam lithography systems were in rapid development. Commercially available PMMA was investigated and lines as narrow as 45 nm were fabricated at Hughes Research Labs [24]. Similar research was also ongoing at IBM, Westinghouse, University of California Berkeley, and Texas Instruments. Conventional tungsten filament cathodes were replaced by lanthanum hexaboride (LaB_6) which provided higher brightness. Laser interferometers began to be used for fine stage motion control. In order to increase throughput Pfeiffer at IBM developed a shaped beam system [25] which exposed an adjustable spot of the resist simultaneously as opposed to pixel-by-pixel exposure of the previous Gaussian beam tools. During this time shaped beam techniques were also independently developed by Carl Zeiss Jena in former East Germany [26].

By the 1980's, specialized lithography systems were commercially available. Wolf showed that aberrations considerably limit the achievable spot size when the beam is deflected off-axis. As opposed to previous EBL systems which used modified scanning electron microscopes (offering high resolution over a field size of 5 µm), these lithography instruments sacrificed ultra-high resolution in order to offer millimeter-sized fields. Researchers also investigated nanometer scale fabrication. They were able to reproduce the resolution of the primary beam by directly dissociating metal fluoride which is insensitive to secondary electrons. Similar resolution was also demonstrated with PMMA resist.

Although these experiments demonstrated the ultimate line-width resolution of electron-beam lithography, many issues were still present and it was very difficult to retain these properties uniformly over large fields. The systems also required lot of user interaction and tweaking; focusing and stigmation of the beam had to be manually adjusted by the operator, fluctuations were hard to correct.

In 1985 JEOL released their JBX5DIIU combining the needs of a lithography system such as pattern generation, 2.5 nm precision deflection, interferometric stage motion control and a bright LaB_6 electron gun emitting a 50 keV beam. The product was able to write ~25 nm structures across an 80 µm field. It was also in the early 80s that research on electron-beam lithography began in Brno at the Institute of Scientific Instruments, Czech Academy of Sciences (then Czechoslovak Academy of Sciences) [14]. A shaped beam system was developed and marketed as the Tesla BS600 series.

In the early 1990s, IBM changed their chip design from bipolar transistors to CMOS-based reducing the required part numbers by several orders of magnitude [26]. This made direct-write electron-beam systems unnecessary and impractical ending the first and only era of large-scale industrial application direct wafer exposure EBL. Bell Laboratories invented SCALPEL in the 1990s solving several problems of projection EBL thus making it feasible [27]. By scattering electrons in the mask as opposed to absorbing them, the active layer of the mask could be made very thin (~100 nm) which also ensured thermal stability. A similar approach was taken by Nikon in cooperation with IBM who developed PREVAIL [28]. In addition to a scattering mask PREVAIL uses variable axis lens to dynamically correct for off-axis aberrations while scanning the beam. LaB_6 electron sources were replaced by thermal field emitters made of tungsten coated with zirconium oxide; these produce very small, bright, stable sources with minimal electron energy spread. Hitachi developed a cell projection lithography system capable of exposing an array of complicated cell patterns in one shot [29]. Here, a cell aperture is selected from the set of available shapes by a deflector, and a variable shaped beam is produced by shaping deflector. Exposing variable shaped and size features in one shot led to an increase in throughput of 1–2 orders of magnitude in the production of quarter micron memories and application specific integrated circuits. In the meantime the semiconductor industry has moved to optical lithography and did not adapt these techniques.

Current research in Europe, the US, and Japan focuses on maskless lithography (ML2) projects [30]. These aim for *massively parallel* projection of pixels. The separation of electrons into several beamlets reduces the beam blur caused by Coulomb interactions between the electrons and allows much higher total currents exposing wafers faster. The proposed systems use 64 to several million beamlets but these projects are in early phases and the demonstrated performance is orders of magnitude below the stated goals.

2.2 Electron-beam Lithography Exposure Methods

Writing directly with an electron beam inherently leads to low writing speeds as all "pixels" of the pattern need to be written by the beam one by one. The simplest lithography systems employing the principles of scanning microscopes scan the substrate with a very narrow Gaussian beam to achieve small feature size with sharp edges as shown in figure 2.1a. Small beam size here results in lengthy exposure times.

The lithography process can be sped up considerably using shaped beams which write much larger areas during a single shot. This is illustrated in figure 2.1b–c. Here the electron source illuminates a square aperture which acts as the object to be demagnified. Further increase in throughput can be achieved by using an aperture of the same shape as the written pattern (figure 2.1d). Another approach is to use many parallel point beams to write the pattern in a single shot (figure 2.1e).

2.3 The Patterning Process

Two methods are used for nanometer-scale EBL pattern generation. The first (figure 2.2) involves spin coating the substrate with a suitable electron resist, such as PMMA. After the electron-beam exposure, the exposed parts of the resist are chemically removed. A metal layer (commonly gold) is deposited on the sample, after which it is submerged in a suitable solvent to remove the unexposed resist together with the unneeded metal layer; this process is referred to as *lift-off*. A several hour

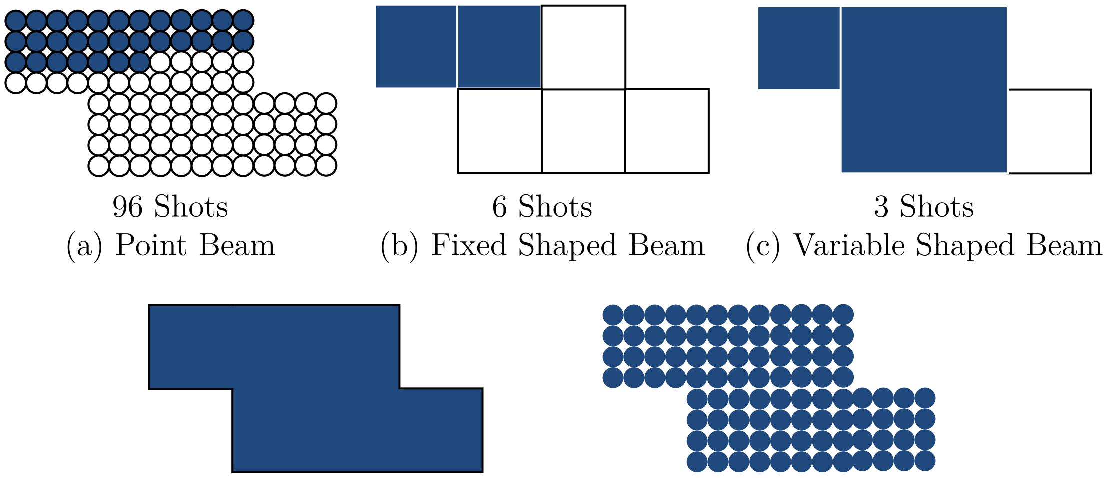

96 Shots
(a) Point Beam

6 Shots
(b) Fixed Shaped Beam

3 Shots
(c) Variable Shaped Beam

1 Shot
(d) Cell Projection

96 Shots at 1 Exposure
(e) Multiple Parallel Beams

Figure 2.1: Comparison of electron-beam lithography exposure methods. Using a conventional point beam, 96 shots are required to write the illustrated pattern. Using a fixed shaped beam reduces the exposure to six shots while a variable shaped beam system only needs 3 shots. A cell projection system can write the pattern in a single shot. Multiple beam systems use several beams parallel beams to write all 96 shots of the pattern at the same time. From [31].

acetone bath is commonly used to dissolve unexposed PMMA. The sample is then cleaned of the PMMA contamination in an ultrasonic cleaner. After the lift-off, the metal layer only remains attached to the substrate in places where it was deposited directly onto it. PMMA in this case acts as a positive resist.

In the second method (figure 2.3), a coherent metal layer is deposited directly on the substrate. The sample is then spin coated with a negative electron resist. After the exposure and development steps, the remaining resist serves as a mask for chemical etching or ion beam sputtering. These remove the unneeded metal areas (and usually disturb the substrate surface). The exposed resist can then be removed chemically leaving only the metallic pattern.

2.4 Competing Techniques

In addition to direct-write EBL and projection EBL discussed in the previous sections, several other techniques allow sub-micron or nanometer scale pattern fabrication.

Nanoimprint lithography (NIL) creates a pattern by mechanical deformation of imprint resist. The main benefit of NIL is its simplicity; there is no need for complex optics or radiation sources with a nanoimprint tool leading to a low cost. Sub 10-nm structures have been manufactured using NIL. The disadvantages of this method include defects caused by trapped air bubbles, non-optimal adhesion between stamp and resist, template wear, etc. [33]

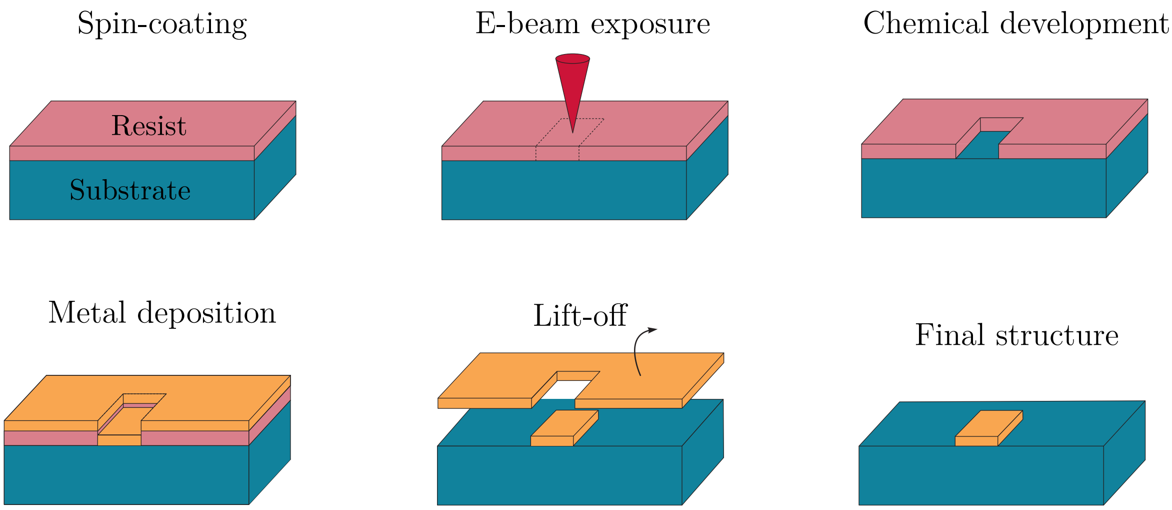

Figure 2.2: The steps of the electron-beam patterning process using lift-off. According to [32].

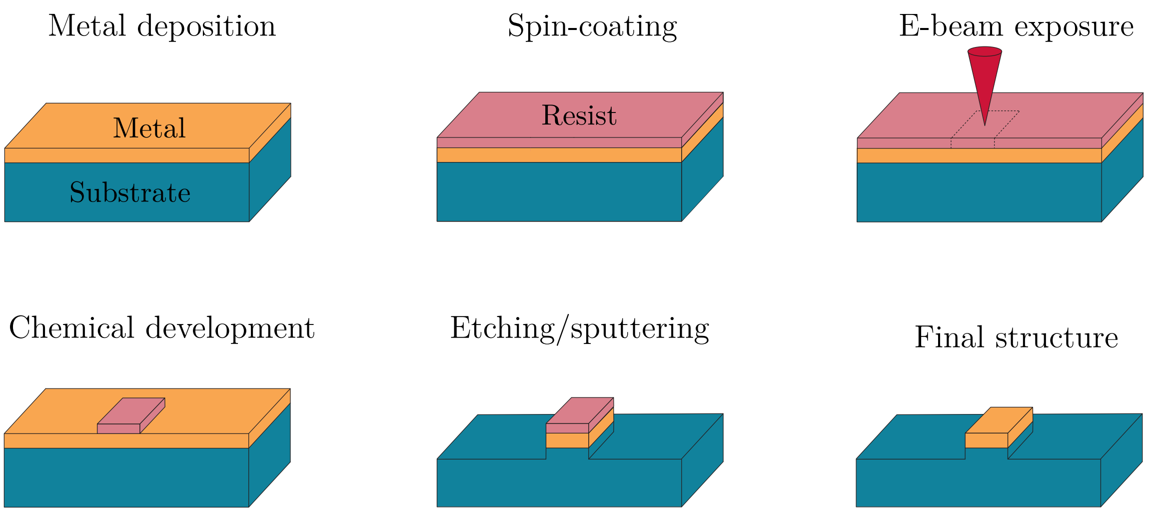

Figure 2.3: The steps of the electron-beam patterning process using chemical etching or ion sputtering. According to [32].

Photolithography (ultra-violet lithography UVL, extreme ultra-violet lithography EUVL) are light projection techniques with very high throughput. UVL is extensively used in the electronics industry nowadays for creating complex integrated circuits such as computer processors and memory chips. Variations of UVL such as immersion lithography and multiple patterning are used to overcome diffraction limits (193 nm wavelength UV light is currently used to manufacture 14 nm half-pitch processors [34]). EUVL is expected to enable even smaller feature sizes in the near future by using a 13.5 nm wavelength light source [35].

X-ray lithography is a projection method using X-rays to transfer a geometric pattern to a light-sensitive resist. Having wavelengths below 1 nm, X-rays overcome the diffraction limits of optical lithography. X-ray lithography is usually operated without magnification or with a slight demagnification offering a resolution around 10 nm [36].

3 TESLA BS600 LITHOGRAPHY SYSTEM

The optical column of the Tesla BS600 electron-beam lithography system was chosen to explore and study the possibilities of dynamic corrections of field curvature, astigmatism, and distortion. The system was designed in Brno at the Institute of Scientific Instruments (ISI) nearly 30 years ago. Today only a handful of these devices remain; one of them is still installed at ISI and still used for research at the time of writing this thesis. The litograph has been upgraded several times during the past decades, these upgrades mainly addressed the quickly aging control system and electronics; the optical elements have remained the same. The following paragraphs briefly summarize the features of the BS600 electron-beam writer.

3.1 Electron-beam Writer Description

As mentioned in section 2.1, research on electron-beam lithography in Brno began in the early 1980s at ISI. This research lead to the development of a lithography system marketed by former company Tesla as the BS600 series. The writer uses a 15 keV variable sized rectangular beam with a spot size of 50–6300 nm. The spot size is adjustable in this interval independently in both directions with a step size of 50 nm.

The optical column of the BS600 is illustrated in figure 3.1a. The column begins with a field emission electron gun operated in the Schottky regime. The cathode is made of a 100 µm diameter monocrystalline tungsten wire with the [100] crystallographic orientation parallel to its axis. The tip is activated with ZrO to lower the work function thus increasing emission current. The cathode is heated by adjustable current to its operating temperature around 1500 K.

The emitted electrons are accelerated toward the extractor electrode with an acceleration potential of 15 kV (the extractor being grounded). The emission current can be adjusted by applying a small negative voltage to the suppressor electrode which is located between the cathode and the extractor. The optimal total emission current is of the order of 10 µA.

After accelerating the beam to the nominal 15 keV energy, a magnetic condenser lens C1 creates the image of the virtual source at the crossover. This is where the beam shaping system is located. As shown in figure 3.1b, the beam first passes through the first square aperture cutting two edges in the beam. The converging beam forms a crossover and then passes through the second square aperture cutting the remaining two edges and creating the rectangular beam which is focused on the substrate. The square apertures are located 17 mm above and below the crossover. A set of electrostatic deflector plates around the beam crossover enables deflecting the beam slightly off-axis. The downstream aperture then cuts the beam to a smaller size which is linearly translated to a smaller spot size on the substrate. The spot size can be independently changed in both x and y directions this way with a step of 50 nm (at the substrate). The deflection system is also used as a beam blanker — by rapidly applying a high voltage pulse to the deflection system, the beam is completely intercepted by the lower aperture and does not expose the electron resist.

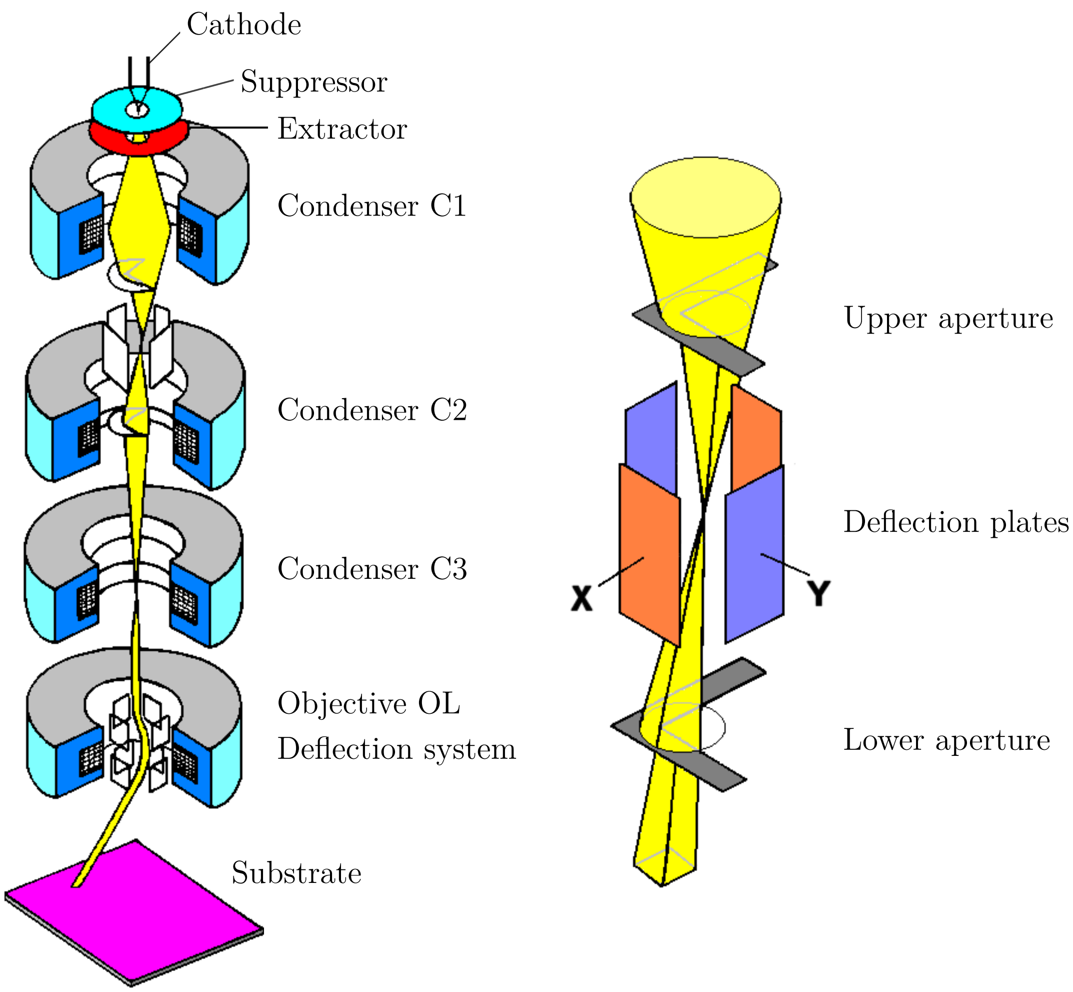

(a) BS600 optical column (b) Shaping system

Figure 3.1: Schematic view of the BS600's optical column (a) showing the electron emission cathode and acceleration electrodes, the four magnetic lenses C1, C2, C3, OL, and the shaping and deflection system. A close-up of the beam shaping system located between C1 and C2 is shown in (b). Features not to scale. From the *BS601 service manual* [37].

The rectangular beam, passing through three magnetic lenses creates the image of the square apertures on the substrate. These are two condenser lenses C2 and C3, and the objective lens OL.

The objective lens bore houses a two-stage magnetic deflection system. Two stages deflecting the beam in opposite directions are used to minimize deflection aberrations. Both stages use a set of two toroidal coils per deflection direction (x and y) per stage. The scanning speed is greatly limited by eddy currents in the casing of the objective when high-frequency deflection signals are applied. To lower the eddy currents, another set of toroidal coils is wound around the deflection system. The current in these coils is the same magnitude as the deflection current signal, flowing in the opposite direction, thus their magnetic field cancels the field of the inner coils. The lower magnetic field around the whole deflection system induces smaller eddy currents in the magnetic objective casing and this allows higher deflection frequencies.

The deflected beam is focused on the substrate by the objective lens. Using the nominal excitation, the lenses form the demagnified image of the beam shaping square apertures on the sample located at the working distance around 40 mm[1] with a magnification of 0.05.

In addition to the mentioned coils and deflectors there are several other optical elements to correct parasitic aberrations introduced by imperfect machining and assembly. Inside condensers C1 and C2 there is a quadrupole stigmator to compensate axial astigmatism and a centering coil to compensate the tilt of the magnetic lenses with respect to the optical axis. Inside the objective lens, just below the deflection system, a pair of coils is installed which provide dynamic focusing capabilities. Dynamic focusing will be discussed in detail in chapter 4.

To maintain a high enough mean free path of the electron beam, the litograph is operated in vacuum. The vacuum vessel encloses the electron gun, the optical axis of the litograph, and the sample. The lowest pressure (ultra-high vacuum, $\sim 10^{-6}$ Pa) is in the electron gun area to ensure its correct operation. This is achieved by using four ion pumps. The magnetic lenses and the deflection system are located outside of the vacuum. The excitation current of all lenses except C1 is around 100–200 mA and these do not require active cooling. The condenser C1 requires a higher current (about 1.8 A) thus needs to be cooled at all times during operation.

3.2 Electron-optical Description

As part of this thesis, a computer model of the BS600 series writer was created in EOD (Electron Optical Design [17]). All components (lenses, deflectors, etc.) were modeled in different input files with at least 300 thousand mesh points in the 2D $r - z$ mesh. Only the optical column from the shaping system downward to the sample was considered. The electron gun and the condenser C1 was not included in the model; it was assumed that these form a crossover at $z = -381$ mm. The beam shaping apertures are then at $z = -398$ mm and $z = -364$ mm. In the shaped beam mode these apertures are the objects to be imaged on the substrate (ideally both in the same image plane with equal magnification), while the crossover needs to be imaged close to the object focal point of the objective lens to ensure homogeneous illumination of the sample placed at $z = 40$ mm.

Several possible combinations of lens excitation exist which provide an acceptable beam path; axial ray trajectories of three well-defined modes starting at the crossover are shown in figure 3.2. In mode 1, the axial ray is parallel to the optical axis between the condenser C3 and the objective lens OL. In mode 2, the axial ray is parallel to the axis after leaving the field of OL. The axial ray ray in mode 3 transverses the objective in such way that its slope remains unchanged. In all of these three modes, the image of the beam shaping apertures is formed at $z \approx 40$ mm, about 0.15 mm apart from each other. In any mode, the apertures are imaged with the same magnification (less then one percent difference), the magnification varies

[1]The working distance WD is the distance between the end of the objective lens downstream pole piece and the substrate surface where the beam is focused.

between 0.044 and 0.066 across the modes. Mode 1 seems the most suitable, as here the demagnification of the apertures can be adjusted by only changing the excitation of C3, and independently the working distance can be modified by tuning the objective excitation. Recently, a new feature has been implemented offering a higher demagnification setting producing a smaller spot while retaining beam current [38]. This was achieved by changing the excitation of C3 in mode 1.

3.3 Gaussian spot

According to the thesis assignment, Gaussian-beam lithography systems were to be studied. When writing with a Gaussian beam, the crossover is imaged on the sample (as opposed to imaging the shaping apertures in case of shaped beams). It is possible to convert the BS600 into a Gaussian-beam system simply by turning off the condenser C2 and leaving the excitation of C3 and OL unchanged. Now the second image of the crossover at $z_o = -381$ mm is formed at $z_i = 40$ mm. With the original C3 excitation of 650 At, the first object of the crossover lies at -151.39 mm. To simplify further calculations, the excitation of C3 has been slightly adjusted to 618.8 At so that the image is formed at $z = -150$ mm. Since modern electron microscopes and lithography systems use much shorter working distances (WD) than the original 40 mm, the WD has been reduced to 5 mm by increasing the excitation of the objective to 1312.55 At. Even at the 60% higher excitation the lens shows no signs of saturation, and the axial flux density is still a linear function of excitation.

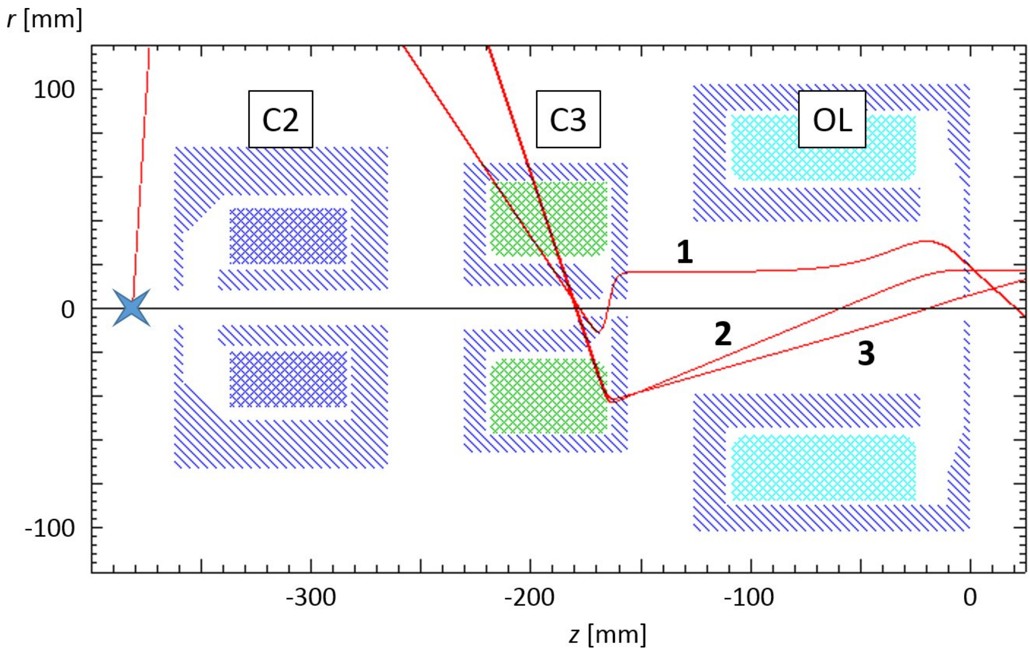

Figure 3.2: Axial rays starting at the crossover (blue cross, $z = -381$ mm) with unit initial angle in three possible modes of the BS600. In all three modes, the image of the beam shaping apertures is formed on the sample at $z \approx 40$ mm, about 0.15 mm apart from each other.

The new WD value 5 mm was chosen to achieve similar capabilities as the Tescan MIRA and LYRA series electron microscopes which are used for lithographic applications at the Institute of Physical Engineering, FME, BUT. These microscopes use a Gaussian beam and offer spot sizes down to ~ 3 nm with a beam current around 200–250 pA. These spot properties can be retained within a $\sim 150 \times 150$ µm^2 field. The commercial lithography system Raith 150 Two offers similar spot parameters, a slightly larger write field of 250×250 µm^2 at the expense of beam current which is limited to around 25 pA.

By lowering the working distance, the uncorrectable aberrations, such as the spherical and chromatic aberration, become smaller. On the other hand, e.g. field curvature increases with decreasing working distance but this can be dynamically corrected as will be shown in the following chapters. The spherical and chromatic aberration of the 5 mm WD setup are 24.5 mm and 23.7 mm, respectively (expressed at the image plane).

The optimal aperture angle can be calculated by minimizing the probe size for the given constraints such as beam current and aberrations. According to Reimer [9], the probe diameter d_p can be expressed as the function of the aperture angle α_p

$$d_p^2 = d_0^2 + d_d^2 + d_s^2 + d_c^2 \tag{3.1}$$

$$d_p^2 = \left[\frac{4I_p}{\pi^2\beta} + (0.6\lambda)^2\right]\alpha_p^{-2} + \frac{1}{4}k_S^2\alpha_p^6 + \left(k_x\frac{\Delta E}{E}\right)^2\alpha_p^2, \tag{3.2}$$

where d_0 is the probe diameter due the probe current I_p and gun brightness β, d_d is the probe diameter due to diffraction of electrons with a wavelength λ, d_s and d_c are the probe diameters due to the spherical k_S and the chromatic k_x aberrations. The function (3.2) is plotted in figure 3.3 for typical properties of a Schottky emitter $\beta = 5 \times 10^{12}$ [Am^{-2}sr^{-1}] and $\Delta E = 0.4$ eV; the probe current is 250 pA, and the beam energy is 15 keV. Minimizing the function (3.2) yields the optimal aperture angle

$$\alpha_{\mathrm{opt}} = 4.5 \text{ mrad} \tag{3.3}$$

in the image plane corresponding to a $d_p = 4.6$ nm spot. Dividing by the angular magnification 67.8, the optimal aperture angle in the object plane at $z_o = -381$ mm is $\alpha_{\mathrm{opt},o} = 66.3$ µrad. This value will be used for evaluation of the properties and aberrations of the EBL system.

3.4 Properties of the Gaussian-spot Mode

The meridional coordinate r of the principal rays w_a and w_b (as defined in equation (1.25)) in the converted Gaussian-mode lithography column are shown in figure 3.4. The condenser C3 and objective OL forms the image of the crossover at $z_o = -381$ mm on the substrate at the working distance $z_i = 5$ mm. The crossover diameter assumed to be 100 nm. C3 and OL are both asymmetrical magnetic lenses with iron casing and pole pieces. Their properties are summarized in table 3.1. The paraxial properties of the imaging system can be found in table 3.2.

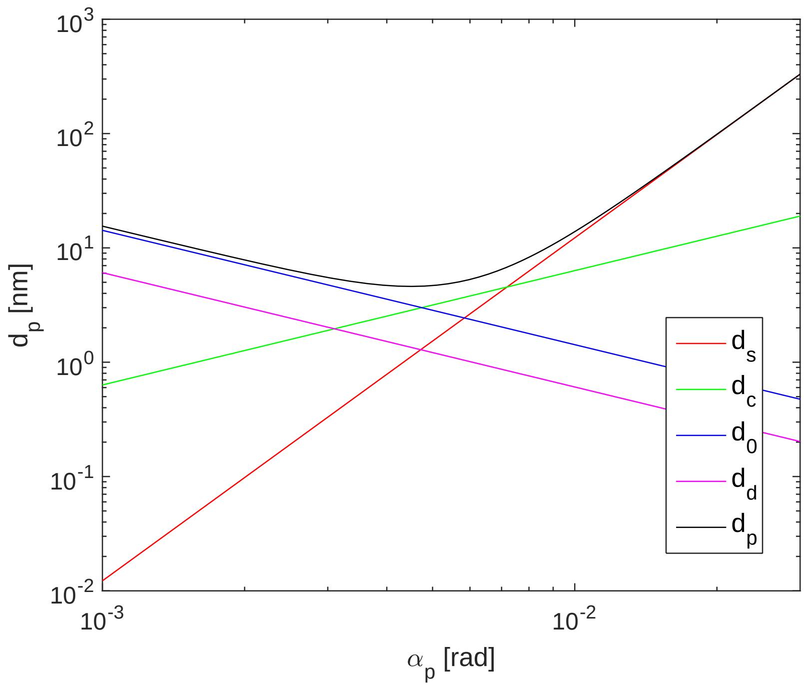

Figure 3.3: Probe size vs. aperture angle. The contribution of the 24.5 mm spherical and 23.7 mm chromatic aberration, the Schottky gun energy spread 0.4 eV and brightness $5{\times}10^{12}$ [$\mathrm{Am^{-2}sr^{-1}}$] forming the 250 pA beam, the diffraction of the 15 keV electrons, as well as the net probe size is shown. The probe size was calculated according to equation (3.2). The optimal aperture angle is 4.5 mrad.

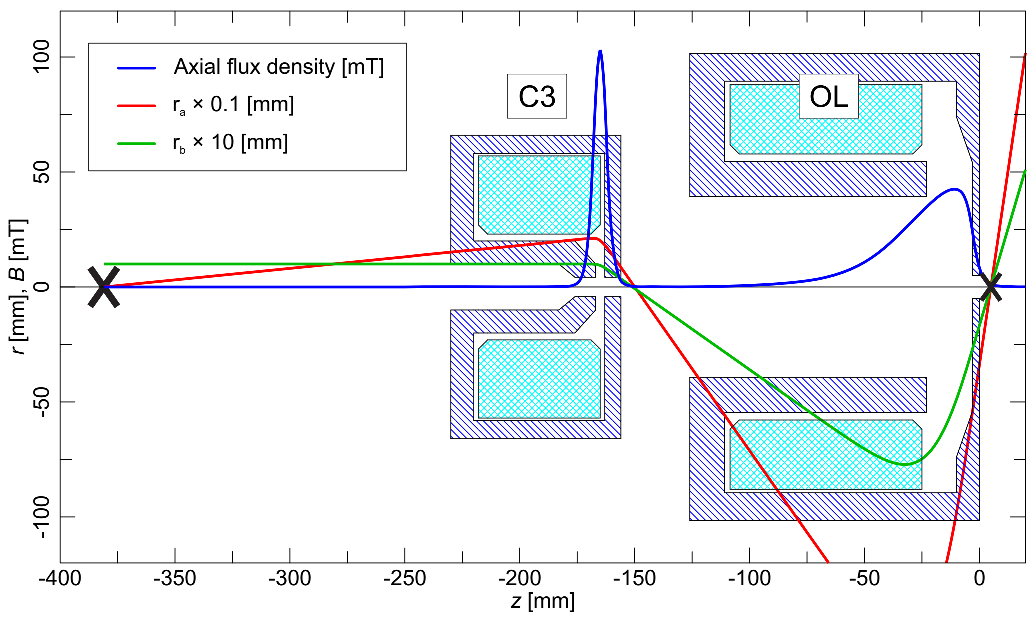

Figure 3.4: The lithography column in the Gaussian-beam mode with the axial flux density and the principal trajectories in the meridional plane r_a, r_b. The crossover ($\times$, $z_o = -381$ mm) is imaged onto the sample at $z_i = 5$ mm (smaller $\times$) by the condenser C3 and objective OL.

Table 3.1: Excitation properties of the condenser C3 and objective OL in the Gaussian-spot 5 mm working distance mode.

	C3	OL
Number of turns [ ]	5000	3700
Current [mA]	124	355
Excitation [A-turns]	618.8	1312.6
Axial field maximum [mT]	103	42.6
Field maximum position [mm]	-165	-10.7
Field width [mm]	7.5	38.2
Object focus z [mm]	-179.0	-35.3
Image focus z [mm]	-151.0	-0.054
Focal length [mm]	14.2	24.1

Table 3.2: Paraxial properties of the lithography column in the Gaussian-spot mode.

	Object (crossover)	Image #1	Image #2 (spot)
Position [mm]	-381	-150	5
Transverse size [nm]	100	7.02	1.47
Aperture angle [mrad]	0.0663	0.945	4.5
Magnification [ ]	1	-0.0702	0.0147
Angular magnification [ ]	1	-14.24	67.8
Beam rotation [rad]	0	0.926	2.88

4 MAGNETIC DEFLECTION AND CORRECTION

Currently, all optical elements of the BS600 series electron-beam writer installed at ISI are magnetic with the exception of the shaping system which uses electrostatic deflection fields. The magnetic lenses, deflection system, stigmators, dynamic focus and centering coils were the obvious choice at the time of the design as high-speed electronics were not available. In addition, magnetic optical elements generally have lower aberrations and act on the electron beam with stronger force than their electrostatic counterparts. This chapter describes the currently used optics of the lithography system modified to produce a narrow Gaussian spot. Special treatment is given to the dynamic correction of field curvature and astigmatism as per the thesis assignment.

4.1 Magnetic Deflection

As described in section 3.1, the BS600 series writer uses a dual-stage magnetic deflector utilizing toroidal coils. Additionally another set of coils is wound around the deflection system to minimize eddy current induction in the objective casing. The deflection system has been modeled in EOD according to the available technical drawings and documentation as shown in figure 4.1. The upper deflectors are wound 7.75 turns, and the lower deflectors 16 turns. The toroidal coils form the optimal angle 60° to eliminate the hexapole field.

The main advantage of a dual-stage deflection system is that a selected aberration can be nullified and the other aberrations considerably decreased. The two possible options are nullifying either the deflection coma or chromatic aberration [14]. Eliminating both aberrations simultaneously is only possible using a three-stage deflector. As both aberrations are complex, eliminating them involves rotating the deflection stages with respect to each other, as well as finding the optimal excitation ratio. The rotation of the stages has not been found in the available documentation, and the provided excitation ratio does not seem to have optimal aberrations; additionally the objective excitation has been altered. Therefore, the ideal parameters of the deflection stages to eliminate coma have been calculated using the simple formula derived from (1.39)

$$K_{L,u}\,\gamma_u + me^{i\varphi}K_{L,l}\,\gamma_l = 0, \tag{4.1}$$

where $K_{L,u}$ and γ_u are the coma and deflection of the upper deflector, $K_{L,l}$ and γ_l are the coma and deflection of the lower deflector, m is the excitation ratio and φ is the rotation of the lower deflection stage. Equation (4.1) has a solution for any arbitrary dual-stage deflection. An analogous equation can be used to eliminate the chromatic aberration. Eliminating coma is usually preferable as it decreases other third-order aberrations as well [39]. The zero-coma condition was chosen in our case as well yielding the optimal excitation and rotation of the lower deflector

$$m = 0.932, \qquad \varphi = -2.31 \text{ rad}. \tag{4.2}$$

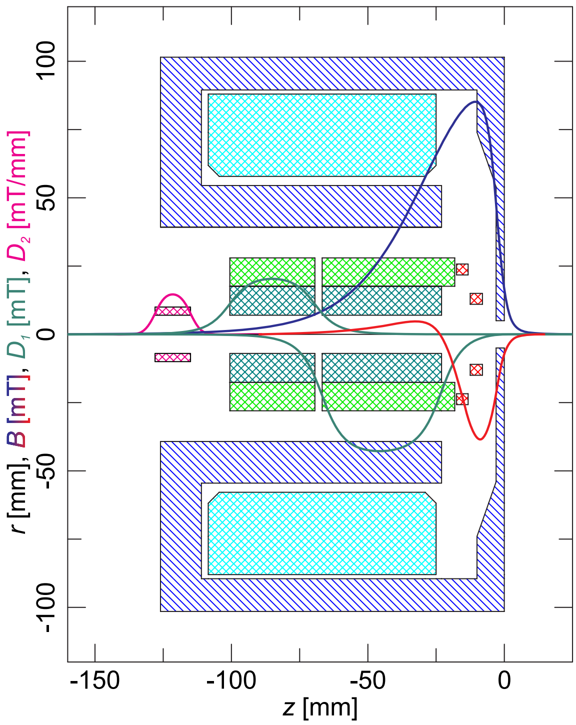

Figure 4.1: Dual-stage magnetic deflection using toroidal coils (green crosshatch) inside the objective lens (blue section lines). Dynamic focus coils (red crosshatch) and an added stigmator (purple) is also shown. The axial field is shown for all components in their color. The OL axial flux density is scaled 2×, the dipole fields of the deflectors for unit current excitation are scaled 500×, the dynamic focus field for unit current excitation is scaled 50×, and the stigmator field is scaled 10×.

In order to deflect the beam in the x direction, both stages have been rotated by 2.20 rad. The same set of coils has been added and rotated by $\pi/2$ rad which deflects the beam in the y direction. The aberration coefficients of the deflection system are summarized in table 4.1.

Table 4.1: Aberration coefficients of the magnetic deflection system related to the image plane.

Coma	K_L^m	[ ]	$6.29\times10^{-5} - 5.42\times10^{-5}\,\mathrm{i}$
Field curvature	K_F^m	[1/mm]	2.16×10^{-2}
Astigmatism	K_A^m	[1/mm]	$1.34\times10^{-2} - 2.75\times10^{-3}\,\mathrm{i}$
Distortion	K_D^m	[1/mm^2]	$-3.25\times10^{-4} - 6.24\times10^{-4}\,\mathrm{i}$
Chromatic	K_T^m	[ ]	$1.49\times10^{-1} - 1.09\times10^{-1}\,\mathrm{i}$

4.2 Dynamic Correction of Field Curvature

The field curvature of the deflection system can be compensated by introducing a dynamic focus coil with excitation proportional to the square of the deflection

$$I^{\mathrm{DF}} \propto \gamma_i \bar{\gamma}_i. \tag{4.3}$$

According to the technical documentation, two dynamic focus coils are already implemented inside the objective lens, below the lower deflection stage as can be seen in figure 4.1; the upper coil has 17 turns and the lower 22 turns excited in the opposite direction. These produce an additional magnetic field superimposed on the objective lens field. The newly introduced field effectively lowers the focusing power of the objective, shifting the curvature plane D in figure 1.2 to the right so that the image is formed on the sample. Two possible methods have been worked out to calculate the optimal excitation of the dynamic focus coils. They involve: 1) using the *Optics–Focus* module of EOD, and 2) calculating the field curvature of the dynamic focus lens using aberration theory.

4.2.1 Focusing with EOD

The *Optics–Focus* module of EOD can be used to calculate the optimal field magnitude and thus excitation of a lens so that it forms the image at a specified location. The field curvature is somewhat equivalent to a defocus changing with radial distance. The optimal defocus Δz is related to the field curvature coefficient K_F^m as

$$\Delta z = z_i - z_{i,\mathrm{Gaussian}} = K_F \gamma_i \bar{\gamma}_i, \tag{4.4}$$

where γ_i is the deflected ray position at the image plane. The z_i image plane is then used as the *Focus* module input. EOD calculates the magnitude of the dynamic focus field for the set deflection. For a $\gamma_i = 0.1$ mm deflection, the optimal defocus and field magnitude m is

$$\Delta z = 216.4 \text{ nm}, \qquad m = 0.001121. \tag{4.5}$$

As the excitation of the dynamic focus coil in EOD is set to the number of turns, the value of m corresponds directly to the optimal excitation current $I_{0.1} = 1.121$ mA. Using (4.3), the excitation current of the dynamic focus coil can be calculated for arbitrary deflection

$$I^{\mathrm{DF}}\ [\mathrm{A}] = \frac{1}{0.1^2}\, I_{0.1}\ [\mathrm{A}]\, \gamma_i \bar{\gamma}_i\ [\mathrm{mm}] = 0.1121\, \gamma_i \bar{\gamma}_i\ [\mathrm{mm}]. \tag{4.6}$$

Introducing the dynamic focus coil can slightly change the field curvature of the system which is used to determine the defocus. In this case, the optimal defocus and excitation can be recalculated from the new field curvature. In reality, the change of field curvature was always negligible.

4.2.2 Aberration Theory

The previous method relies on the advanced optimization feature of EOD which might not be available for all systems. Zhu et al. had derived the optimal dynamic correction excitation currents for shaped beam lithography systems in [16]. Their calculation uses the non-relativistic approximation. Inspired by this paper, the relativistically correct relations have been derived using aberration theory.

In the paraxial equation (1.24) we set $F_1 = D_1 = 0$. The original axial magnetic flux density B_0 is modified by the introduced dynamic focus field B_c to $B = B_0 + B_c$. The paraxial equation is then written as

$$\begin{aligned} w'' + \left(\frac{\gamma\phi'}{2\phi^*} - \mathrm{i}kB_0\right) w' + \left(\frac{\gamma\phi''}{4\phi^*} - \frac{\mathrm{i}k}{2}B_0'\right) w = P, \\ P = \mathrm{i}kB_c w' + \frac{\mathrm{i}k}{2}B_c' w. \end{aligned} \tag{4.7}$$

Setting the right-hand side of (4.7) zero, the homogeneous solutions are the paraxial trajectories w_a and w_b. The additional terms on the right-hand size of equation (4.7) can be treated using the variation of parameters method, not unlike the derivation of aberrations in chapter 1. The particular solution is

$$w_p = a(z)w_a + b(z)w_b. \tag{4.8}$$

$a(z)$ and $b(z)$ can be expressed as

$$a(z) = \frac{1}{W}\int_{z_o}^{z} P\bar{w}_b\sqrt{\Phi^*}\,\mathrm{d}\zeta, \qquad b(z) = -\frac{1}{W}\int_{z_o}^{z} P\bar{w}_a\sqrt{\Phi^*}\,\mathrm{d}\zeta, \tag{4.9}$$

where $W = \sqrt{\Phi^*(z_o)} = \sqrt{\Phi^*(z_i)}\,MM_a$ is the *Wronskian.* The general solution is $w = \alpha_o w_a + \beta_o w_b + a(z)w_a + b(z)w_b$, and the ray position difference from the homogeneous solution in the object plane is given by the only nonzero term

$$\Delta w(z_i) = -\frac{w_b(z_i)}{W}\int_{z_o}^{z_i} P\bar{w}_a\sqrt{\Phi^*}\,\mathrm{d}z, \tag{4.10}$$

as $w_a(z_i) = 0$. The field curvature is proportional to α_o, therefore we substitute the trajectory $w = \alpha_o w_a$ into the term P of equation (4.10). Using $w_b(z_i) = M\exp(\mathrm{i}\theta)$, the position difference Δw can then be expressed using object-related aberration coefficients as

$$\Delta w(z_i) = Me^{\mathrm{i}\theta}k_{Fo}^{\mathrm{DF}}\alpha_o\gamma_o\bar{\gamma}_o = -\frac{\alpha_o Me^{\mathrm{i}\theta}}{W}\int_{z_o}^{z_i}\left(\mathrm{i}kB_c w_a' + \frac{\mathrm{i}k}{2}B_c' w_a\right)\bar{w}_a\sqrt{\Phi^*}\,\mathrm{d}z, \tag{4.11}$$

from which it is evident that the field curvature of the dynamic focus coil k_{Fo}^{DF} is

$$k_{Fo}^{\mathrm{DF}} = -\frac{1}{\gamma_o\bar{\gamma}_o W}\int_{z_o}^{z_i}\left(\mathrm{i}kB_c w_a' + \frac{\mathrm{i}k}{2}B_c' w_a\right)\bar{w}_a\sqrt{\Phi^*}\,\mathrm{d}z. \tag{4.12}$$

To compensate the field curvature K_{Fo}^{m} of the deflectors, the net ray shift of the two curvatures needs to be zero

$$mMe^{\mathrm{i}\theta}k_{Fo}^{\mathrm{DF}}\alpha_o\gamma_o\bar{\gamma}_o + Me^{\mathrm{i}\theta}K_{Fo}^{m}\alpha_o\gamma_o\bar{\gamma}_o = 0, \tag{4.13}$$

where m is the magnitude of the unit-current dynamic focus coil field. The zero net field curvature condition is then

$$m = -\frac{K_{Fo}^{m}}{k_{Fo}^{\mathrm{DF}}}. \tag{4.14}$$

Writing $k_f = k_{Fo}^{\mathrm{DF}}\gamma_o\bar{\gamma}_o$, where k_f is not a function of γ_o, it is evident that the dynamic focus field magnitude is proportional to the square of the deflection

$$m = -\frac{K_{Fo}^{m}}{k_f}\gamma_o\bar{\gamma}_o. \tag{4.15}$$

In order to calculate the field curvature of the dynamic focus coil, the w_a trajectory and the axial flux density were exported from the EOD model with a 0.01 mm step. Equation (4.12) was numerically integrated in MATLAB using the trapezoidal rule. The primed terms were calculated by differentiating the cubic spline interpolation. The resulting field curvature for a unit-current excitation is

$$k_{Fo}^{\mathrm{DF}}\gamma_o\bar{\gamma}_o = -888.2 \text{ mm}, \quad \text{or} \tag{4.16}$$

$$k_{Fo}^{\mathrm{DF}}\gamma_i\bar{\gamma}_i = -0.193 \text{ mm} \tag{4.17}$$

The deflection field curvature expressed in the object plane is equal to the image curvature in the image plane $K_{Fo}^{m} = K_{F}^{m} = 0.0216 \text{ mm}^{-1}$; the optimal magnitude of the dynamic focus field is then

$$I^{\mathrm{DF}} \text{ [A]} = m = 2.431\times 10^{-5}\ \gamma_o\bar{\gamma}_o \text{ [mm]}, \quad \text{or} \tag{4.18}$$

$$I^{\mathrm{DF}} \text{ [A]} = 0.1119\ \gamma_i\bar{\gamma}_i \text{ [mm]}. \tag{4.19}$$

Again, m is equal to the excitation current I^{DF} in amperes.

Comparison

The optimal excitation current of the dynamic focus coil was calculated with two different approaches. Calculating the optimal defocus and focusing the beam slightly further using EOD's *Optics–Focus* module, the optimal current is

$$I^{\mathrm{DF}} \text{ [A]} = 0.1121\, \gamma_i\bar{\gamma}_i \text{ [mm]}. \tag{4.20}$$

Deriving the additional field curvature of the dynamic focus coil using aberration theory resulted in the optimal current expressed as

$$I^{\mathrm{DF}} \text{ [A]} = 0.1119\ \gamma_i\bar{\gamma}_i \text{ [mm]}. \tag{4.21}$$

The two methods yield a different optimal excitation by 2‰ which is a good agreement considering the great amount of numerical calculations involved.

Modifying the axial flux density of the objective lens by the addition of the dynamic focus coils influence the paraxial properties of the system. Important aspects are how well the magnification is preserved, and how the beam rotation (meridional plane rotation) changes. Figure 4.2 shows how the dynamic focus coil affects these properties. The effects are quadratic and can be described by

$$\Delta\theta\ [\text{mrad}] = -1.10\,\gamma_i\bar{\gamma}_i\ [\text{mm}], \tag{4.22}$$
$$\delta M\ [‰] = \quad 1.68\,\gamma_i\bar{\gamma}_i\ [\text{mm}]. \tag{4.23}$$

The change in magnification is less than 1‰ for the considered write fields and can be neglected. However, as the dynamic focus coils are below the deflection stage, the deflected beam rotates around the optical axis differently by the additional dynamic focus field. This results in additional deflection distortion — a transverse shift of the deflected spot in the image plane. The shift is approximately equal to

$$\Delta w(z_i) = \gamma_i\bar{\gamma}_i\left(e^{\mathrm{i}\Delta\theta} - 1\right), \tag{4.24}$$
$$|\Delta w(z_i)| = \gamma_i\bar{\gamma}_i\,|\Delta\theta|\,. \tag{4.25}$$

For 500 µm deflection, the spot is shifted by $|\Delta w(z_i)| \approx 70$ nm.

4.3 Dynamic Correction of Astigmatism

The astigmatism of the deflection system can be compensated by introducing a dynamic stigmator with excitation proportional to the square of the deflection

$$I^{\text{st}} \propto \gamma_i^2. \tag{4.26}$$

The stigmators present in BS600 (in C1 and C2) cannot be used to eliminate the astigmatism with realistic current magnitude. A new stigmator was therefore introduced in the optical column, just before the upper deflection stage as shown in figure 4.1. In accordance with [40], the stigmator has 200-turns saddle coils in 20°

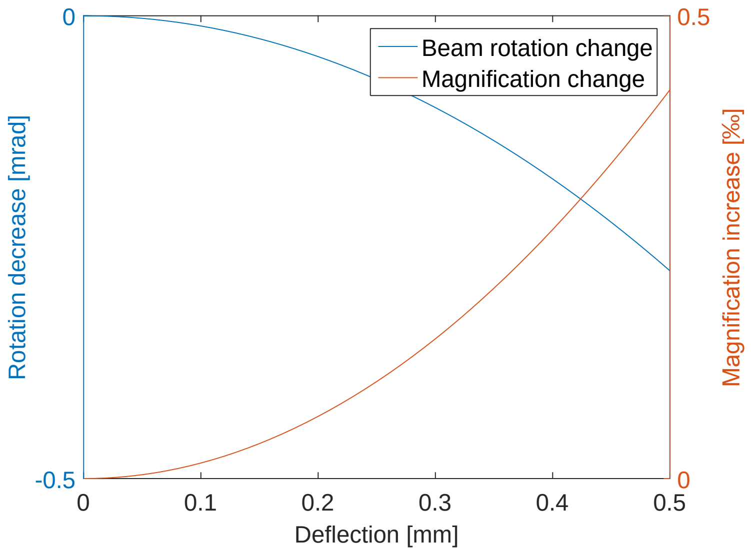

Figure 4.2: The effect of the dynamic focus coil on the rotation of the beam and the magnification.

angle creating a quadrupole field as shown in figure 1.11. The practical excitation current limit for such a stigmator is around 50 mA [40]. The saddle coils are 13 mm long and are wound on a cylinder with a 7 mm radius; their quadrupole field D_2 has a maximum axial field of 1.46 mT/mm for unit excitation current located at $z = -121.5$ mm. The field width is 13.5 mm.

Again, two possible ways have been worked out to calculate the astigmatism of the dynamic stigmator, and to determine its optimal excitation and rotation. The first method relies on calculating the astigmatism by fitting the spot of a ray-traced beam. In the second method, the introduced astigmatism was calculated using aberration theory.

4.3.1 Fit

One possible way of determining the astigmatism of the newly introduced stigmator is using ray-tracing and fitting. Several particles are traced from the crossover at $z_o = -381$ mm . The initial angle of these particles was tangential to the edge of a circular aperture, $|\alpha_o| = i/n\,\alpha_{\max}$, where $\alpha_{\max}$ is the optimal-probe-diameter aperture angle 66.3 µrad calculated in 3.3, $i = 1, 2, \ldots, n$, and n was set to 5. The image of such rays form in the aperture plane before the lenses is 5 circles. After passing through the lenses and the stigmator, the rays form ellipses in image plane z_i. The shape of the ellipses is determined by the spherical aberration and astigmatism of the system. Knowing the initial parameters of the rays and the paraxial properties of the system, the aberrations forming the shapes of the ellipses can be calculated using a least-squares fit method. The ray tracing was performed in EOD, and the fitting in MATLAB.

The axial astigmatism calculated from the fit for unit-current excitation of the stigmator is

$$k_A^{\text{fit}} = 1.783\times10^4 - 5.348\times10^3\,\mathrm{i}\ \text{mm} \tag{4.27}$$

with a standard deviation of $15 + 15\mathrm{i}$ mm. To eliminate the deflection astigmatism, the contributions of the two astigmatisms need to cancel each other

$$mMe^{i\theta}k_{Ao}^{\text{fit}}\bar{\alpha}_o + Me^{i\theta}K_{Ao}^{m}\bar{\alpha}_o\gamma_o^2 = 0, \tag{4.28}$$

where m is the complex magnitude of the quadrupole field. Solving for m one gets

$$m = -\frac{K_{Ao}^{m}}{k_{Ao}^{\text{fit}}}\gamma_o^2 \tag{4.29}$$

$$m = (7.33\times10^{-7} + 6.58\times10^{-8}\,\mathrm{i})\,\gamma_o^2\ [\text{mm}] \tag{4.30}$$

$$m = (2.76\times10^{-3} + 1.97\times10^{-3}\,\mathrm{i})\,\gamma_i^2\ [\text{mm}]. \tag{4.31}$$

The astigmatism expressed in the object and image planes is equal $K_A^m = K_A^m$. It is evident, that the dynamic stigmator quadrupole field needs to be rotated with changing deflection γ. The quadrupole field can be arbitrarily rotated by superimposing two stigmators rotated 45° as described in 1.11. For the sake of simplicity, only the physical rotation of the stigmator has been implemented in the EOD model. The real field magnitude μ and the rotation of the stigmator field χ is given by

$$\mu = |m|, \qquad \chi = \arg(m)/2. \tag{4.32}$$

The factor 1/2 is the consequence of the fact that a rotation of the stigmator by χ rotates the quadrupole field D_2 by 2χ; $D_2^* = D_2 \exp(2\mathrm{i}\chi)$ [16].

4.3.2 Aberration Theory

While ray tracing in the previous method offers a simple solution, it is much more elegant to derive the astigmatism introduced by the addition of the dynamic stigmator. The validity of both methods can then be confirmed if the results are the same.

The steps of the derivation are very much the same as in case of the field curvature calculation in section 4.2.2. The term P appearing on the right-hand side of the paraxial equation (4.7) in this case is

$$P = -\left(2kD_2 + \frac{\gamma}{\Phi^*}F_2\right)\bar{\alpha}_o\bar{w}_a, \tag{4.33}$$

where D_2 is the quadrupole field of the magnetic stigmator, and F_2 is the electric quadrupole field (not present in this case). The ray position shift due to the introduced astigmatism in the image plane is

$$\Delta w(z_i) = Me^{\mathrm{i}\theta}k_{Ao}^{\mathrm{st}}\bar{\alpha}_o\gamma_o^2 = \frac{\bar{\alpha}_o Me^{\mathrm{i}\theta}}{W}\int_{z_o}^{z_i}\left(2kD_2 + \frac{\gamma}{\Phi^*}F_2\right)\bar{w}_a^2\sqrt{\Phi^*}\,\mathrm{d}z. \tag{4.34}$$

The stigmator astigmatism is then equal to

$$k_{Ao}^{\mathrm{st}} = \frac{1}{\gamma_o^2 W}\int_{z_o}^{z_i}\left(2kD_2 + \frac{\gamma}{\Phi^*}F_2\right)\bar{w}_a^2\sqrt{\Phi^*}\,\mathrm{d}z. \tag{4.35}$$

To eliminate the net astigmatism, the sum of the deflection and the stigmator astigmatism must be zero

$$mMe^{\mathrm{i}\theta}k_{Ao}^{\mathrm{st}}\bar{\alpha}_o\gamma_o^2 + Me^{\mathrm{i}\theta}K_{Ao}^m\bar{\alpha}_o\gamma_o^2 = 0, \tag{4.36}$$

where m is the complex magnitude of the quadrupole field which is equal to the excitation current in amperes. Solving for m

$$m = -\frac{K_{Ao}^m}{k_{Ao}^{\mathrm{st}}}. \tag{4.37}$$

Writing $k_a = k_{Ao}^{\mathrm{st}}\gamma_o^2$, where k_a is not a function of γ_o, it is evident that the stigmator field magnitude is proportional to the square of the deflection

$$m = -\frac{K_{Ao}^m}{k_a}\gamma_o^2. \tag{4.38}$$

The calculation of k_{Ao}^{st} was performed using the same method as in section 4.2.2. The resulting astigmatism for a unit-current excitation is

$$k_{Ao}^{\mathrm{st}}\gamma_o^2 = -4.630\times 10^3 - 1.537\times 10^4\,\mathrm{i}\ \mathrm{mm}, \quad \text{or} \tag{4.39}$$

$$k_{Ao}^{\mathrm{st}}\gamma_i^2 = -1.572 + 3.113\mathrm{i}\ \mathrm{mm}. \tag{4.40}$$

The optimal (complex) excitation of the dynamic stigmator is then

$$m = \left(-7.732\times10^{-8} + 8.495\times10^{-7}\,\mathrm{i}\right)\gamma_o^2\ [\mathrm{mm}], \quad \text{or} \tag{4.41}$$

$$m = \left(-2.436\times10^{-3} + 3.079\times10^{-3}\,\mathrm{i}\right)\gamma_i^2\ [\mathrm{mm}], \tag{4.42}$$

The real excitation magnitude and the physical rotation of the stigmator can then be calculated as

$$\mu = |m|, \qquad \chi = \arg(m)/2 - \pi/4. \tag{4.43}$$

The field of the dynamic stigmator calculated by EOD is not in the basic direction as is assumed by the calculation, the stigmator therefore needs to be rotated by additional $-\pi/4$ rad. The (real) excitation current of the rotated stigmator in amperes is then equal to μ.

Comparison

The optimal excitation current and rotation of the dynamic stigmator was calculated with using two different methods. The first method relies on calculating the stigmator's astigmatism by fitting the spot image formed by the introduced quadrupole field. The fitted value was then compared with the deflection astigmatism to get the optimal complex magnitude of the stigmator field

$$m = (2.76\times10^{-3} + 1.97\times10^{-3}\,\mathrm{i})\,\gamma_i^2\ [\mathrm{mm}]. \tag{4.44}$$

The real field magnitude μ (which is equal to the excitation current I^{st} in amperes), and the rotation of the stigmator χ can be written as

$$I^{\mathrm{st}}\ [\mathrm{A}] = \mu = |m|, \qquad \chi = \arg(m)/2. \tag{4.45}$$

For a 0.1 mm deflection in the x direction these formulas yield

$$\boldsymbol{I^{\mathrm{st}}\ [\mathrm{A}] = \mu = 33.9\times10^{-6}}, \qquad \boldsymbol{\chi = -1.261\ \mathrm{rad}}. \tag{4.46}$$

Deriving the additional astigmatism of the dynamic stigmator using aberration theory resulted in the optimal complex field magnitude expressed as

$$m = \left(-2.436\times10^{-3} + 3.079\times10^{-3}\,\mathrm{i}\right)\gamma_i^2\ [\mathrm{mm}], \tag{4.47}$$

The excitation current I^{st}, and the rotation of the stigmator χ is then

$$I^{\mathrm{st}}\ [\mathrm{A}] = \mu = |m|, \qquad \chi = \arg(m)/2 - \pi/4. \tag{4.48}$$

For a 0.1 mm deflection in the x direction these formulas yield

$$\boldsymbol{I^{\mathrm{st}}\ [\mathrm{A}] = \mu = 39.3\times10^{-6}}, \qquad \boldsymbol{\chi = -1.261\ \mathrm{rad}}. \tag{4.49}$$

The excitation current of the stigmator calculated by the two methods differs by 14% while the optimal stigmator rotation is different by no more than 1‰.The derived stigmator excitation produces a circular spot while the fitting method's result is slightly elliptical. It can be therefore concluded that the usage of the fitting method is questionable and the treatment using aberration theory is justified and provides more accurate results.

4.4 Dynamic Correction of Distortion

The deflection distortion and the distortion introduced by the additional dynamic focus and dynamic stigmator fields has no effect on spot size; the spot is merely shifted in the image plane. As the compensation of these distortions is, in principle, the same as using electrostatic deflection and correctors, it will be treated in chapter 5.

4.5 The Corrected System

The optimal excitation of the dynamic focus coils and the dynamic stigmator has been derived. Here, their influence on the spot calculated by ray tracing is discussed. The sequence of pictures in figure 4.3 illustrates how the 0.1 mm deflected spot changes after applying the optimal dynamic corrections. As expected, the field curvature correction reduces the spot size in the sample plane and the astigmatism correction eliminates its ellipticity. Furthermore, after applying the dynamic stigmator field, the spot remains circular in all planes close to the substrate as shown in figure 4.4. The spot is larger behind the sample plane than before due to the spherical aberration.

The effect of deflection magnitude on beam spot properties has been studied and is summarized in table 4.2. The spot remains circular with unchanged diameter up to about 500 µm deflection. After, its size increases and becomes elliptical. If a 17% increase in diameter and a slight ellipticity is accepted, the beam can be deflected up to 700 µm corresponding to a 1×1 mm^2 write field. At greater deflections the spots of different energies are laterally shifted by chromatic aberration; at 700 µm deflection, the shift is 1.8 nm.

Figure 4.5 shows the geometrical spot after correction of the field curvature, astigmatism, and distortion for the nominal energy $E_0 = 15$ keV and for energies $E_0 - dE/2$ and $E_0 + dE/2$, where $dE = 0.4$ eV. In reality, the current density is concentrated around the center of the spot, its effective size is closer to the nominal energy spot.

Table 4.2: The effect of deflection on spot size after dynamic corrections. The spot diameter was calculated for nominal beam energy.

Deflection [µm]	Write field [µm^2]	Major diameter [nm]	Minor diameter [nm]	Diameter increase %
0	N/A	4.4	N/A	0
100	140x140	4.4	N/A	0
200	280x280	4.4	N/A	0
300	420x420	4.4	N/A	0
500	700x700	4.6	N/A	4
700	1000x1000	5.5	4.8	17

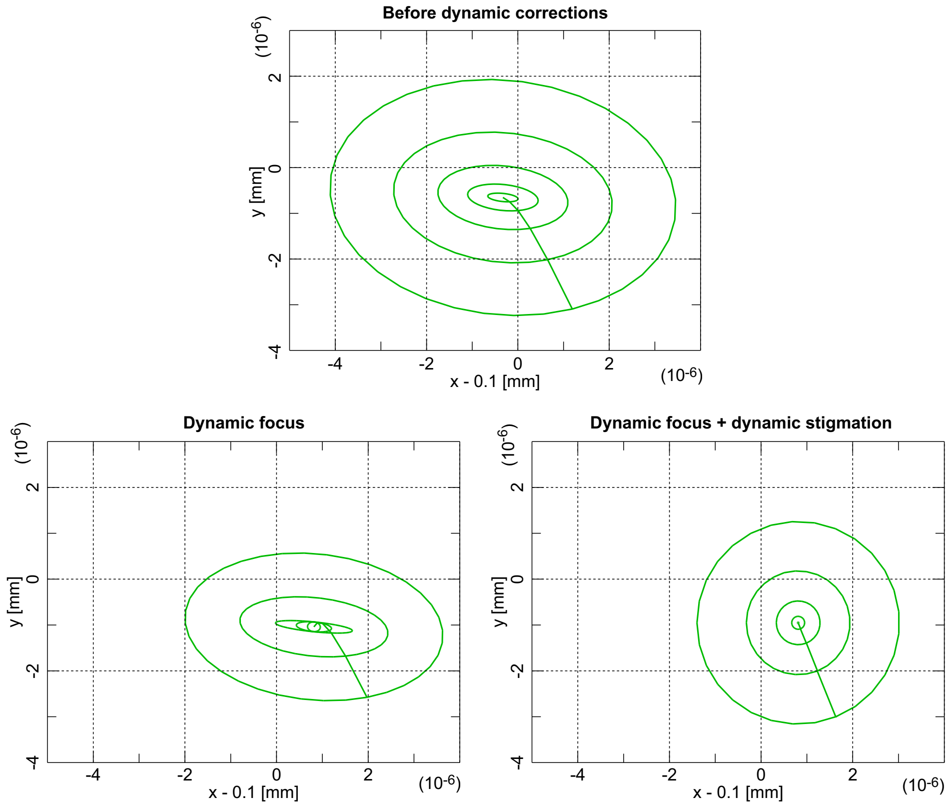

Figure 4.3: Change in 0.1 mm deflected spot size and shape after applying the dynamic focus to eliminate field curvature and the dynamic stigmation to eliminate deflection astigmatism. The ellipses correspond to 5 equidistant initial angles up to the optimal aperture angle α_{opt}. The dynamic focus decreases the spot size in the sample plane, and the astigmatism correction compensates its ellipticity. Dynamic correction of distortion is not applied here.

4.6 Summary

In this chapter, the dynamic correction of the field curvature and astigmatism of the current toroidal magnetic dual-stage deflection system was treated using several methods. The BS600 electron-beam writer already has two dynamic focus coils inside the objective lens, just below the lower deflection stage, as shown in figure 4.1. A magnetic stigmator was added to the setup above the upper deflection stage. The stigmator is composed of 200-turn saddle coils at a distance of 7 mm from the optical axis, and its quadrupole field has a maximum at $z = -121.5$ mm. The optimal excitation current of the stigmator for 0.1 mm deflection is on the order of microamperes, the number of turns can therefore be reduced to for example 5. Then, the optimal current is several milliamperes.

In order to calculate the optimal excitation of the dynamic correction devices. their influence on the aberrations was evaluated for unit-current excitation. The optimal excitation was then calculated so that the newly introduced field compensates the aberrations of the magnetic deflectors. Two methods have been worked out for the determining the optimal excitations for both field curvature and astigmatism

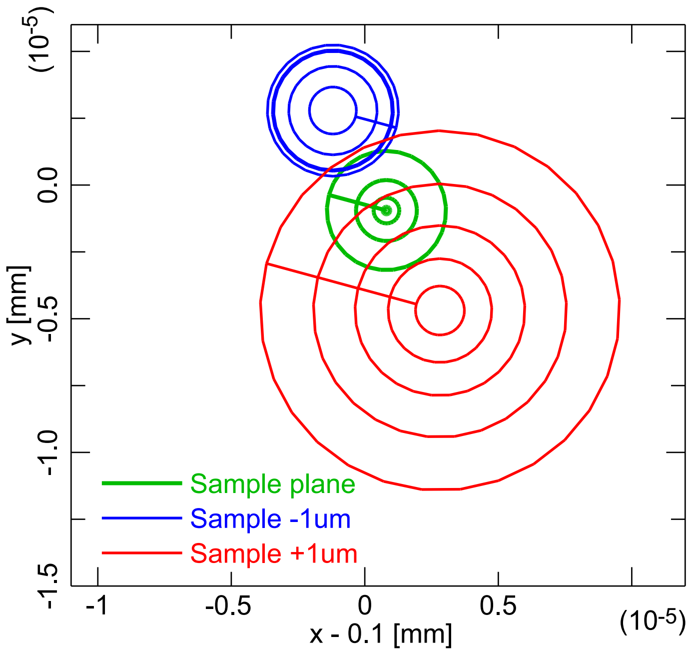

Figure 4.4: Dynamically corrected 0.1 mm deflected spot in planes 0.1 µm before and after the sample plane. The astigmatism correction completely eliminates the spot ellipticity.

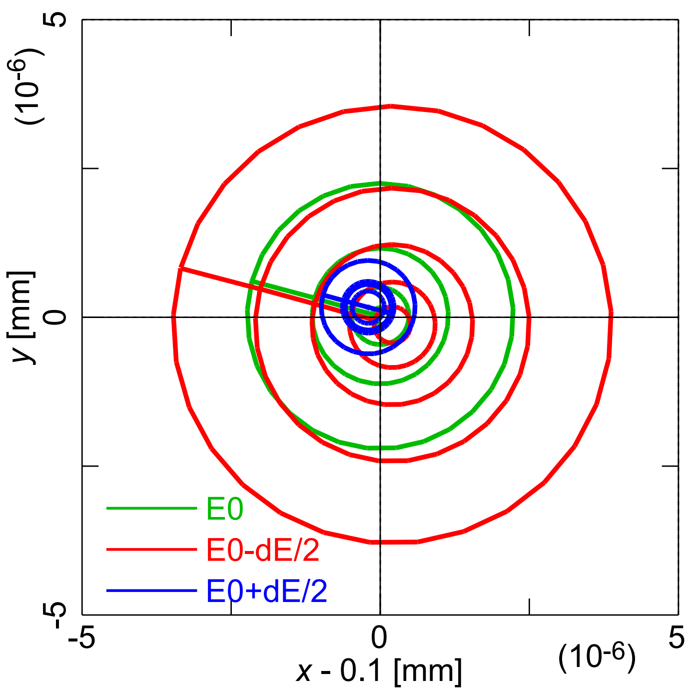

Figure 4.5: The effect of chromatic aberration illustrated on a 0.1 mm deflected beam of energies close to the nominal energy 15 keV. The energy spread dE is 0.4 eV. The field curvature, astigmatism, and distortion are corrected. The circles correspond to 5 equidistant initial ray angles up to the optimal aperture angle α_{opt}.

correction.

The dynamic corrections have been applied in the EOD model of the lithography system, and their functionality has been confirmed by calculating the spot properties before and after the corrections. Images of the spots can be found in the previous sections. It was found that the beam retains its circularity and its diameter remains around 4.6 nm up to 500 µm deflection. Deflecting 700 µm, the spot becomes slightly elliptical and its diameter increases by 17%.

5 ELECTROSTATIC DEFLECTION AND CORRECTION

The main goals of this thesis was to design an electrostatic deflection system and compare its properties to the current magnetic deflectors. The magnetic electron lenses C3 and OL of the BS600 series electron-beam writer remain unchanged. In this chapter a new electrostatic deflection system is designed, and the dynamic correction of its field curvature, astigmatism, and distortion using electrostatic devices is studied and compared with the magnetic system described in chapter 4.

5.1 Electrostatic Deflection

When designing the electrostatic system, the constraints such as the inner bore diameter of the objective lens had to be taken into account. Dual stage deflectors offer a lower aberrations [41], so only these were considered. In the end, the chosen approach was to stay as close to the dimensions of the original magnetic deflectors as possible so that their properties and aberrations can be compared. An important aspect of the electrostatic deflector design is that the applied voltages must not allow breakdown discharges between the electrodes. Several breakdown mechanisms exist and the breakdown voltages have been extensively studied. In high vacuum used in electron microscopy, at pressures around 10^{-4}–10^{-2} Pa the breakdown voltage between parallel plates was measured by Ilić et al. [42] to be about 45 kV/mm. In electron microscopy, usually much lower voltages are used; the limit in this thesis was set 10 times lower.

As shown in figure 1.8, electrostatic deflectors are usually made of cylindrical equisectored or non-equisectored electrodes. It is important that the deflectors do not produce higher order multipole fields. The most typical design uses 8 electrodes. Non-equisectored 20-electrode deflectors offer higher dipole field homogeneity [43] but involve much more effort to machine and align the electrodes precisely. Therefore only 8-electrode deflectors were considered. Another important aspect is the number of voltage supplies needed per deflection direction. To eliminate the hexapole field, 8-electrode deflectors use two voltages per deflection direction while in a non-equisectored 20-electrode deflection system a single voltage supply is sufficient as shown in figure 1.8. Dual stage systems can be designed such way that a single voltage supply is connected to both stages, this was also taken into account during the design.

Within equisectored 8-electrode deflection systems, the design of figure 1.8(a) was preferred over 1.8(b) as the produced dipole field per unit voltage is about 10% stronger [14]. The designed deflection electrodes are 35° wide and have a 10° separation. To compensate the lower deflection force of electrostatic deflectors, the electrodes were placed closer to the optical axis than the original magnetic deflection coils; at a radial distance of 4 mm. The whole dual stage deflection system is enclosed in metallic casing at ground potential. It limits the deflection field width so that nearby components do not influence each other, and can be also useful for installing the deflectors in the objective lens bore.

The lower deflector stage takes the place of the current lower magnetic stage and has approximately the same length, 45 mm. The separation between the stages and the length of the upper stage is the result of an optimization process. The goal was to eliminate the deflection coma using a single voltage supply for the two stages. The optimal voltage and rotation of the upper stage of an initial design was calculated according to equation (4.1). The two parameters were adjusted in the EOD model, the new field was calculated, and a sufficient design was found iteratively. The deflection coma was lowered to $k_L^e = -4.25\times10^{-5} + 3.45\times10^{-5}\,\mathrm{i}$ this way. The optimal stage separation and upper stage length is 7.5 mm and 5 mm, respectively, as can be seen in figure 5.1. The rotation of the upper stage with respect to the lower stage is −0.708 rad. To deflect only in the x direction, both stages have been additionally rotated by 1.44 rad. The deflection sensitivity is 6.666 µm/V allowing 1 mm deflection with a relatively low voltage of 150 V. The aberrations of the designed deflector are summarized in table 5.1. At this point it can be said that the aberrations of the electrostatic deflector are not that much different than the original magnetic listed in table 4.1. The field curvature, distortion, and the chromatic aberration are slightly higher here; of these, only the chromatic aberration is not compensable dynamically. The designed electrostatic deflection system inside the OL bore is shown in figure 5.1. Mainly electron-optical properties of the deflector design were considered; machining and installation aspects have not been addressed. The construction considerations involved in the design of electrostatic deflectors is thoroughly described in Vlček's dissertation dealing with the design of a Wien-filter [44].

Table 5.1: Aberration coefficients of the electrostatic deflection system related to the image plane.

Coma	K_L^e	[ ]	$-4.25\times10^{-5} - 3.45\times10^{-5}\,\mathrm{i}$
Field curvature	K_F^e	[1/mm]	6.82×10^{-2}
Astigmatism	K_A^e	[1/mm]	$3.78\times10^{-2} - 1.28\times10^{-3}\,\mathrm{i}$
Distortion	K_D^e	[1/mm^2]	$8.89\times10^{-5} - 5.81\times10^{-4}\,\mathrm{i}$
Chromatic	K_T^e	[ ]	$4.87\times10^{-1} + 5.18\times10^{-2}\,\mathrm{i}$

5.2 Dynamic Correction of Field Curvature

The compensation of the deflection field curvature can be accomplished either by lowering the objective lens focusing power dynamically (directly lowering the OL excitation current or introducing a small diverging lens inside the OL), or adjusting the position of the object imaged by the OL — the beam crossover at $z = -150$ mm. Dynamically adjusting the focusing power (excitation current) of the objective lens is not feasible at deflection frequencies, and introducing an electrostatic lens inside the OL field would considerably change the beam rotation due to the changing electron energy inside the magnetic field; these two possibilities have therefore not

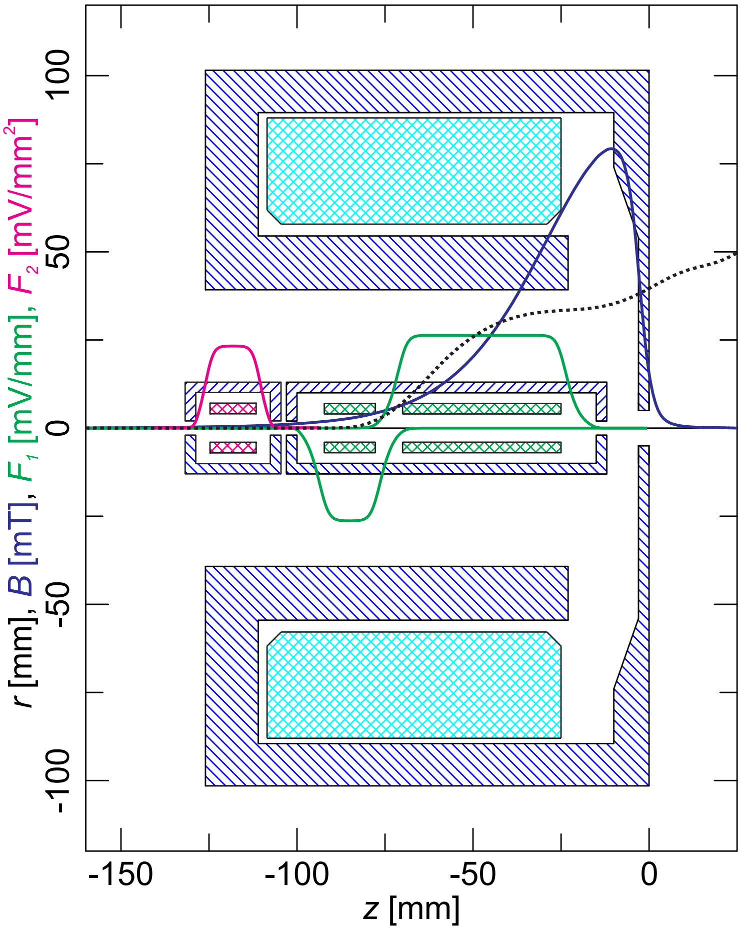

Figure 5.1: The designed electrostatic dual-stage deflector electrodes (green crosshatch) and their casing (blue section lines) inside the objective lens bore. The proposed stigmator is also shown (purple crosshatch). The axial field of the deflector stages (green, scaled 0.1×), the stigmator (purple, scaled 0.3×) and the objective lens (blue, scaled 2×) are plotted as well as the deflected trajectory w_e (black dotted line) scaled to 50 mm deflection.

been studied. The other option is moving the crossover further from the OL towards the electron gun. Several possibilities arise here:

I A diverging lens inserted between the crossover and the objective lens moves the apparent position of the crossover further.

II The objective lens focusing power may be lowered permanently so that the beam is focused behind the sample. A converging lens inserted between the crossover and the OL would then provide the additional focusing. In this case, the dynamic focus lens would be turned off when writing at the write-field edge and turned on when writing near the optical axis.

III A converging lens before the crossover would move it so that the beam is ultimately focused behind the sample with the optimal defocus. Here, two possibilities were studied: dynamic focus lens inside the condenser C3 and before C3.

To study these options, a simple unipotential lens has been designed and placed at the appropriate position. The lens model as well as its axial potential for unit voltage on the central electrode are shown in figure 5.2 left. The positions I, II, IIIa, and IIIb are illustrated in figure 5.3.

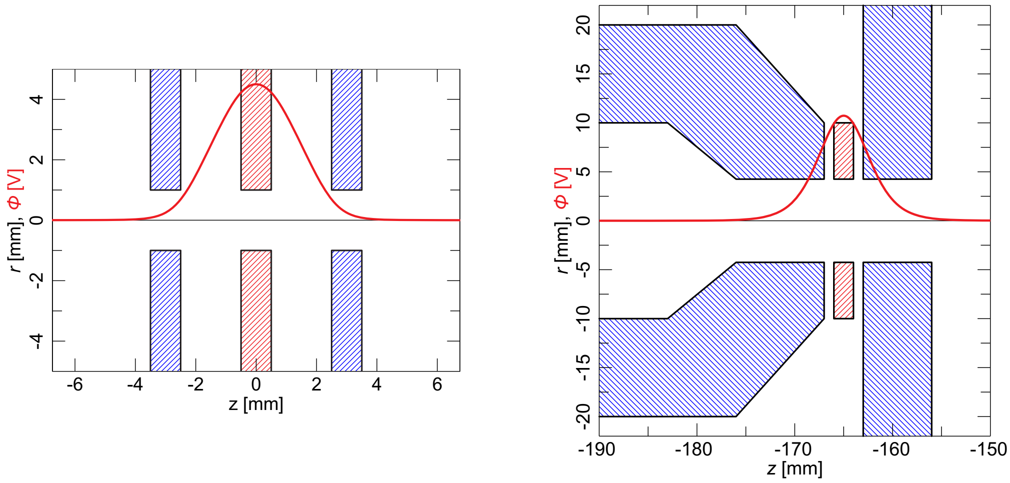

Figure 5.2: Electrostatic lens models used for dynamic focusing: a generic unipotential lens (left; axial potential scaled 5×) and a unipotential lens inside the condenser gap (right axial potential scaled 25×).

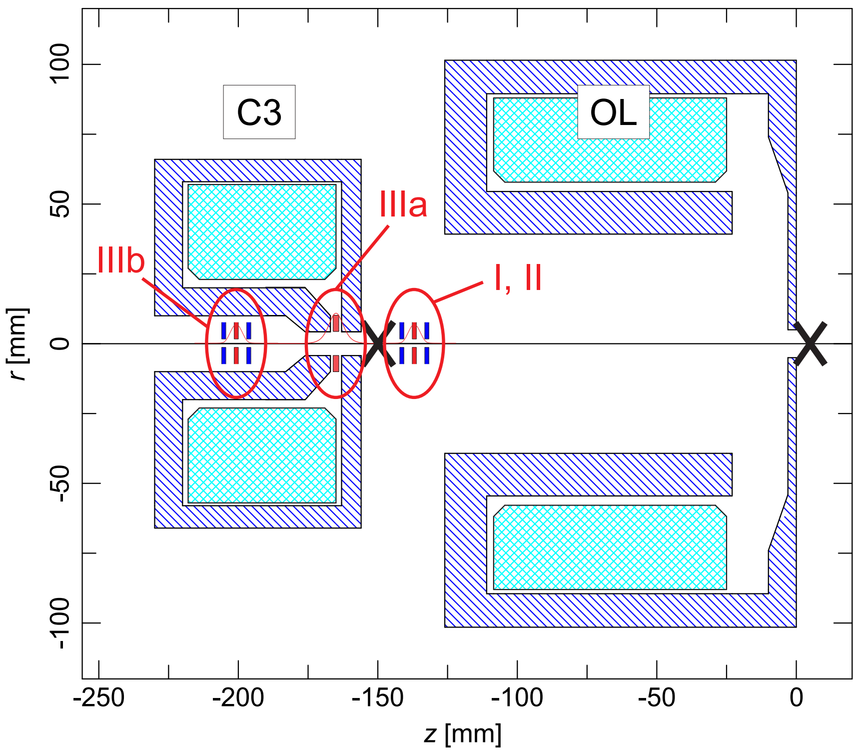

Figure 5.3: Locations of the dynamic focus lenses considered for field curvature correction. Black crosses denote the positions of the crossovers.

I Diverging Lens

At first, the unipotential lens was placed between the crossover ($z = -150$ mm) and the objective lens; at $z = -140$ mm. Having a very high potential ratio of the electrodes, it is possible to construct a unipotential diverging lens. The method using EOD's *Optics–Focus* module was used as described in section 4.2.1 to estimate the optimal potential on the central electrode. The outer electrodes were on the beam potential (15 kV). For a 100 µm deflection ($\Delta z = 216.4$ nm defocus), the optimal potential for the central electrode was found to be 382 kV in accelerating mode, and -1.61 kV in decelerating mode. In decelerating mode, the beam energy drops to around 50 V at the center of the lens. The spherical aberration of the system increases twice in accelerating mode and 20 times in decelerating mode. The very high voltage requirements render using a diverging lens for dynamic focusing not feasible.

II Lowering the OL Focusing Power

Another possibility for dynamic focusing is to set a maximum write field and lower the objective lens excitation so that it focuses the beam on the sample at the edge of the write field. Now, for smaller deflections the beam is focused behind the sample which can be compensated by introducing a weak converging lens between the crossover at $z = -150$ mm and the OL. The same unipotential lens as in option I was used here, placed at $z = -140$ mm. The *Optics–Focus* method described in section 4.2.1 can be employed to calculate the optimal potential of the focusing electrode of the dynamic focus lens. The optimal voltage has also been derived using aberration theory in section 5.2.1.

III Converging Lens Before the Crossover

The object being imaged by the OL — the beam crossover — can be moved further towards C3 by a converging lens placed before the crossover. There isn't enough space between the condenser C3 casing and the crossover at $z = -150$ mm to place an additional lens. The remaining options are (a) designing a lens directly inside the C3 gap or (b) placing the lens in before C3 (either inside the magnetic lens bore or before it).

In case (a), the overlapping electrostatic and magnetic field of the two lenses causes additional beam rotation but since this happens before the deflectors where the beam is axial and circular, it has no effect on the beam spot in the image plane. This solution would affect the spot if the shaped beam were to be used; the rectangular spot would be tilted due to the extra rotation. A weak converging unipotential lens was designed simply by inserting an electrode inside the magnetic lens gap utilizing the pole pieces of C3 as the outer electrodes. The lens and its axial potential for unit voltage on the central electrode is shown in figure 5.2 right.

In case (b), the converging lens used in options I and II is placed between the crossover at $z_o = -381$ mm and the condenser. It decreases the axial ray slope and thus its transverse velocity before the ray enters the C3 field. As the focusing magnetic force of the condenser is proportional to the transverse electron velocity, the smaller-slope ray is focused less. It was found that the lower focusing power of the magnetic lens dominates over the effect of the converging lens. A lens in front of the condenser cannot move the crossover in the negative z direction and therefore cannot provide dynamic focusing. A possible solution is to increase the excitation of the condenser so that the crossover is moved to the left of -150 mm and the image is formed at the sample plane for a nonzero deflection. The dynamic focus coil can then be used to provide the additional focusing for smaller deflections, much like in option II. The optimal field magnitude of the dynamic focus lens is calculated analogously.

5.2.1 Aberration Theory

To eliminate the field curvature of the system, the field curvature of the introduced dynamic focus lens needs to be calculated. Similarly to section 4.2.2, the additional field curvature of the lens was derived using aberration theory. Here, focusing and potentially overlapping electric and magnetic fields have been taken into account. In the paraxial equation (1.24), we set $F_1 = D_1 = 0$ and write $\phi = \phi_0 + \phi_c$, where ϕ_0 is the axial potential of the system without the dynamic focus lens and ϕ_c is the axial potential change introduced by the dynamic focus field. The relativistically corrected potential is then

$$\phi^* = \phi_0^* \left(1 + \frac{\phi_c^*}{\phi_0^*}\right). \tag{5.1}$$

For small correction potentials, the paraxial equation terms including ϕ^* can be approximated by the first order Taylor-series expansion terms

$$\frac{1}{\phi^*} = \frac{1}{\phi_0^*} - \frac{\phi_c^*}{\phi_0^{*2}}, \tag{5.2}$$

$$\frac{1}{\sqrt{\phi^*}} = \frac{1}{\sqrt{\phi_0^*}} \left(1 - \frac{\phi_c^*}{2\phi_0^*}\right). \tag{5.3}$$

Substituting these terms into the paraxial equation and arranging the terms containing the correction potential ϕ_c^* on the right-hand side we get

$$w'' + \left(\frac{\gamma\phi_0'}{2\phi_0^*} - \frac{\mathrm{i}\eta B}{\phi_0^{*2}}\right) w' + \left(\frac{\gamma\phi_0''}{4\phi_0^*} - \frac{\mathrm{i}\eta B'}{2\phi_0^{*2}}\right) w = Q_1 w' + Q_2 w, \tag{5.4}$$

$$Q_1 = \frac{\gamma\phi_0'}{2\phi_0^{*2}}\phi_c^* - \frac{\gamma}{2\phi_0^*}\phi_c' - \frac{\mathrm{i}\eta B}{2\phi_0^{*3/2}}\phi_c^*, \tag{5.5}$$

$$Q_2 = \frac{\gamma\phi_0''}{4\phi_0^{*2}}\phi_c^* - \frac{\gamma}{4\phi_0^*}\phi_c'' - \frac{\mathrm{i}\eta B'}{4\phi_0^{*3/2}}\phi_c^*, \tag{5.6}$$

where we used the approximations $(\phi_0' + \phi_c')\,\phi_c^* \approx \phi_0'\phi_c^*$ and $(\phi_0'' + \phi_c'')\,\phi_c^* \approx \phi_0''\phi_c^*$. The homogeneous equation is the paraxial equation for the original ϕ_0 potential and its solutions are the w_a and w_b rays. The non-homogeneous equation can be solved using the variation of parameters method. The ray position shift of the particular solution in the image plane is

$$\Delta w(z_i) = \frac{M e^{\mathrm{i}\theta}}{W} \int_{z_o}^{z_i} - \left(Q_1 w_a' + Q_2 w_a\right) \bar{w}_a \sqrt{\phi_0^*}\,\mathrm{d}z. \tag{5.7}$$

Attributing Δw to the field curvature $Me^{\mathrm{i}\theta}k_{Fo}^{\mathrm{DF}}\alpha_0\delta_o\bar{\delta}_o$, we substitute $w = \alpha_o w_a$, $w' = \alpha_o w_a'$ into Q_1 and Q_2. The field curvature is then

$$k_{Fo}^{\mathrm{DF}} = -\frac{1}{\delta_o\bar{\delta}_o W}\int_{z_o}^{z_i}(Q_1 w' + Q_2 w)\,\bar{w}_a\sqrt{\phi_0^*}\,\mathrm{d}z. \tag{5.8}$$

Using the approximations

$$\begin{aligned}\gamma &= 1 + 2\varepsilon\phi_0\left(1 + \frac{\phi_c}{\phi_0}\right) \approx 1 + 2\varepsilon\phi_0,\\ \phi_c^* &= (1 + \varepsilon\phi_c)\phi_c \approx \phi_c\end{aligned} \tag{5.9}$$

it is easily seen that the dynamic focus lens field curvature k_{Fo}^{DF} is a linear function of the correction field magnitude. To eliminate the deflection field curvature K_{Fo}^e, the magnitude m of the dynamic focus field needs to satisfy

$$m = -\frac{K_{Fo}^e}{k_{Fo}^{\mathrm{DF}}}. \tag{5.10}$$

As in case of magnetic dynamic focus coil, the correction field magnitude is proportional to the square of the deflection

$$m = -\frac{K_{Fo}^e}{k_f}\delta_o\bar{\delta}_o, \tag{5.11}$$

where $k_f = k_{Fo}^{\mathrm{DF}}\delta_o\bar{\delta}_o$ is not a function of δ_o.

Field curvature correction using the in-gap lens (option IIIa)

The optimal voltage of the dynamic focus lens inside the condenser gap (IIIa) was calculated using the dervid formulas. Integrating the expression (5.8) numerically, the field curvature k_{Fo}^{DF} for unit voltage is

$$k_{Fo}^{\mathrm{DF}}\delta_o\bar{\delta}_o = -6.803\times 10^{-2}\ \mathrm{mm}^{-1}. \tag{5.12}$$

The optimal magnitude of the dynamic focus field is equal to the voltage in volts

$$U^{\mathrm{DF}}\ [\mathrm{V}] = m = 1.002\,\delta_o\bar{\delta}_o, \tag{5.13}$$

$$U^{\mathrm{DF}}\ [\mathrm{V}] = 4.611\times 10^3\,\delta_i\bar{\delta}_i. \tag{5.14}$$

The central electrode potential has to be set at 15 kV $+\,U^{\mathrm{DF}}$, for the correction of a 0.1 mm deflected ray's field curvature it is 15 046.1 V. This dynamic focus lens can only work in accelerating mode. In decelerating mode, the velocity of beam electrons decreases and so does the magnetic focusing Lorentz force. The condenser's lower focusing power dominates over the extra focus of the dynamic focus lens. The crossover is therefore shifted in the wrong direction, towards the objective.

Field curvature correction using the defocused objective (option II)

The decrease of the objective lens focusing power causing a shift of the image plane Δz_f is related to the maximum deflection $\delta_{\max}$

$$\Delta z_f = K_F^e \delta_{\max} \bar{\delta}_{\max}, \tag{5.15}$$

The optimal objective excitation current can be found using EOD's *Optics-Focus* module. The dynamic focus lens in figure 5.2(a) placed between the objective lens and the condenser is then used to focus the beam on the sample for all deflections up to the edge of the writing field $\delta_{\max}$. The optimal potential of the lens's focusing electrode can be calculated by the *Optics-Focus* module as described for magnetic dynamic focusing in section 4.2.1. It was found that the focus potential is proportional to the deflection; for 200 µm maximal deflection: For 200 textmu m maximal deflection, the objective lens excitation is 1312.47 A-turns and the optimal dynamic focus lens potential is

$$U^{\mathrm{DF}}\ [\mathrm{V}] = 1183.6\,(\delta_{\max} - |\delta_i|) \tag{5.16}$$

in accelerating mode, and

$$U^{\mathrm{DF}}\ [\mathrm{V}] = -1095.1\,(\delta_{\max} - |\delta_i|) \tag{5.17}$$

in decelerating mode. The electrode potential is then set to 15 kV + U^{DF}. As the potential of the lens electrode is relatively high, this option of dynamic focusing will not be treated, and option IIIa will be used in further calculations.

5.3 Dynamic Correction of Astigmatism

An 8-electrode electrostatic dynamic stigmator has been designed according to figure 1.10. The electrodes are 13 mm long and are enclosed in a grounded casing. The stigmator was placed just above the upper deflection stage as shown in figure 5.1. The quadrupole field of the stigmator has a peak value of 78 mV/mm^2 for unit electrode potential at $z = -118.5$ mm, the field width is 15.3 mm.

The formulas to calculate the astigmatism introduced by a dynamic stigmator and its optimal field magnitude used for the treatment of magnetic stigmators (4.35) hold for electrostatic stigmators as well. Here,

$$k_{Ao}^{\mathrm{st}} \delta_o^2 = \quad 4.810 + 15.860\,\mathrm{i}\ \mathrm{mm}, \quad \text{or} \tag{5.18}$$

$$k_{Ao}^{\mathrm{st}} \delta_i^2 = -1.777\times 10^4 + 7.417\times 10^4 \mathrm{i}\ \mathrm{mm}. \tag{5.19}$$

The optimal (complex) electrode potential of the dynamic stigmator is then

$$m = \left(7.769\times 10^{-5} + 2.409\times 10^{-3}\,\mathrm{i}\right) \delta_o^2\ [\mathrm{mm}], \quad \text{or} \tag{5.20}$$

$$m = (-5.291 + 9.747\,\mathrm{i})\,\delta_i^2\ [\mathrm{mm}], \tag{5.21}$$

The electrode voltage and the rotation of the stigmator field can then be calculated as

$$U^{\mathrm{st}}\ [\mathrm{V}] = |m|, \qquad \chi = \arg(m)/2. \tag{5.22}$$

The electrode voltages V_a and V_b according to figure 1.10(c) are then

$$V_a = U^{\mathrm{st}} \cos(2\chi), \qquad V_b = U^{\mathrm{st}} \sin(2\chi). \tag{5.23}$$

5.4 Dynamic Correction of Distortion

The deflection distortion shifts the spot position in the image plane without changing its size. Additionally, the dynamic focus lens and the dynamic stigmator may introduce further distortions.

Deflection Distortion

The image shift due to the deflection distortion is given by $k_D^e \delta_i^2 \bar{\delta}_i$ which can be compensated by superimposing a small correction onto the deflection signal. The correction deflection δ_c must satisfy

$$\delta_c + k_D^e \delta_c^2 \bar{\delta}_c = -k_D^e \delta_i^2 \bar{\delta}_i. \tag{5.24}$$

The term containing δ_c^3 is small compared to the others and can be neglected. The correction of the deflection is then directly given by

$$\delta_c = -k_D^e \delta_i^2 \bar{\delta}_i, \tag{5.25}$$

from which the complex correction voltage $U_c = U_{c,x} + \mathrm{i}U_{c,y}$ can be calculated using the deflection sensitivity u

$$U_c = \frac{\delta_c}{u}, \text{ where } \quad u = 6.666 \text{ µm/V}. \tag{5.26}$$

Dynamic Focus Lens Distortion

The effect of the dynamic focus lens on distortion can be easily calculated using aberration theory. Let us take the paraxial equation (5.4) originally derived to calculate the dynamic focus field curvature. This time, the we substitute the deflected trajectory $w = \delta_o w_e$ into on the right-hand side terms. The ray shift in the image plane due to the particular solution is then

$$\Delta w(z_i) = Me^{\mathrm{i}\theta} k_{Do}^{\mathrm{DF}} \bar{\delta}_o \delta_o^2 = \frac{\delta_o M e^{\mathrm{i}\theta}}{W} \int_{z_o}^{z_i} -\Big(Q_1(\phi_c) w_e' + Q_2(\phi_c) w_e\Big) \bar{w}_a \sqrt{\phi_0^*}\, \mathrm{d}z. \tag{5.27}$$

It can be easily seen that the ray shift due to the dynamic focus coil field ϕ_c is nonzero only in case the dynamic focus field overlaps the deflected trajectory. In all discussed options of electrostatic dynamic focusing, the corrector lens was located upstream of the stigmator and their fields did not overlap. The distortion due to the introduction of the dynamic focus lens is therefore zero in all cases.

Dynamic Stigmator Distortion

Using aberration theory, the first-order effect of the dynamic stigmator on distortion can be derived. We take the paraxial equation (4.7) with the right-hand side derived for the dynamic stigmator (4.33). This time, the we substitute the deflected trajectory $w = \delta_o w_e$ into P to get

$$w'' + \left(\frac{\gamma\phi'}{2\phi^*} - \mathrm{i}kB_0\right) w' + \left(\frac{\gamma\phi''}{4\phi^*} - \frac{\mathrm{i}k}{2} B_0'\right) w = P, \tag{5.28}$$

$$P = -\left(2kD_2 + \frac{\gamma}{\Phi^*}F_2\right)\bar{\delta}_o\bar{w}_e. \tag{5.29}$$

The ray shift in the image plane due to the particular solution is

$$\Delta w(z_i) = Me^{i\theta}k^{st}_{Do}\bar{\delta}_o\delta_o^2 = \frac{\bar{\delta}_o Me^{i\theta}}{W}\int_{z_o}^{z_i}\left(2kD_2 + \frac{\gamma}{\Phi^*}F_2\right)\bar{w}_e\bar{w}_a\sqrt{\Phi^*}\,\mathrm{d}z. \tag{5.30}$$

It is evident from equation (5.30) that the dynamic stigmator contributes to the overall distortion only if the quadrupole field F_2 (or D_2 for that matter) overlap the deflection field (or in general, with the deflected trajectory w_e). In the modeled electrostatic deflection and correction system, the stigmator field and the deflection field do not overlap as can be seen in figure 5.1. The voltage on the stigmator electrodes does not affect the spot position in the image plane. This result has been confirmed by ray tracing. A hundredfold increase of the stigmator field magnitude shifted the deflected ray by mere 15 pm, well below the error level of the tracing.

The distortion introduced by the dynamic stigmator needs to be taken into account in systems where $F_2\bar{w}_e \neq 0$. The validity of (5.30) has been confirmed by shifting the stigmator into the dipole field of the deflectors and comparing the results of the derived formula with the results of ray tracing. The stigmator field was shifted 40 mm so that the quadrupole and upper dipole field maxima were nearly coincidental. The deflection was set to 200 µm. The integral (5.30) was evaluated with these parameters; the resulting shift of the deflected ray per unit stigmator voltage was

$$\Delta w_{\mathrm{der}}(z_i) = 19.205 + 41.804\mathrm{i}\ \mathrm{nm}. \tag{5.31}$$

With ray tracing, the obtained shift was

$$\Delta w_{\mathrm{rt}}(z_i) = 19.200 + 41.804\mathrm{i}\ \mathrm{nm}. \tag{5.32}$$

The relative difference between the two results was less than 10^{-4} confirming the validity of the derived stigmator-induced distortion.

Third-order Dynamic Stigmator Distortion

In order to estimate the effect of third-order aberrations of the dynamic stigmator on the distortion (and other aberrations) of the system, a derivation method similar to the previous calculations was employed.

The electrostatic potential is given by the expansions (1.14)–(1.16). Terms up to the third order in w are taken and substituted into the trajectory equation (1.8). From the magnetic potential expansion, only the rotationally symmetrical terms are considered (1.19). After lengthy algebraic manipulations involving neglecting high-order terms, the paraxial equation (1.23) is obtained with additional terms of w and F_2 on the right-hand side

$$\begin{aligned} P_{F2} = \frac{\gamma}{2\phi^*}\Bigg[& -\frac{1}{4}w\bar{w}F_2'' - \frac{1}{12}w^3F_2'' + \frac{\gamma}{8\phi^*}w\phi''\left(\bar{w}^2F_2 + w^2\bar{F}_2\right) - \\ & -\frac{\gamma}{2\phi^*}\bar{w}\left(\bar{w}^2F_2^2 + w^2F_2\bar{F}_2\right) - w'\bar{w}'wF_2\Bigg] - \\ & -\frac{\mathrm{d}}{\mathrm{d}z}\left[\frac{\gamma}{4\phi^{*1/2}}\left(\bar{w}^2F_2 + w^2\bar{F}_2\right)w'\right] \end{aligned} \tag{5.33}$$

The transverse shift of the ray in the image plane is expressed by

$$\Delta w(z_i) = -\frac{Me^{\mathrm{i}\theta}}{W} \int_{z_o}^{z_i} P_{F2} \bar{w}_a \sqrt{\phi^*}\, \mathrm{d}z. \tag{5.34}$$

The standard definition of the deflection distortion is $k^e_{Do}\delta_o^2\bar{\delta}_o$, however, for example Hawkes considers all terms containing $\delta_o^n\bar{\delta}_o^{3-n}, n = \{0, 1, 2, 3\}$ as distortion [45]. The deflected trajectory $w = \delta_o w_e$ is substituted into equation (5.33). Again, it is evident, that the third-order distortion manifests only if the quadrupole field F_2 and the deflected trajectory w_e overlap.

Considering all terms according to Hawkes and moving the stigmators 40 mm towards the deflection stages to increase the effect of the quadrupole field, a 500 µm deflected ray is shifted by the unit-potential stigmator by

$$\Delta w(z_i) = -84.2 - 563\mathrm{i}\ \mathrm{pm}. \tag{5.35}$$

This low value of the shift could not be confirmed as it is on the limit of the ray tracing error, and for these high values of deflection and stigmator voltage other effects are dominant, such as the linear stigmator distortion described in section 5.4. It is safe to say that the third-order stigmator distortion does not affect the spot position considerably.

5.5 The Corrected System

Hitherto, the dynamic correction of field curvature, astigmatism, and distortion of the designed electrostatic deflection system was treated. In this section, the effects of these correctors on the spot size and shape is demonstrated. The series of spots in figure 5.4 shows the studied dynamic corrections of on a 0.1 mm electrostatically deflected beam spot. The electrostatic dynamic focus lens inside the condenser gap eliminates field curvature thus decreasing the spot size; the stigmator compensates deflection astigmatism and removes the spot ellipticity; and the distortion correction moves the spot to the paraxial deflection position. Similarly to the astigmatism-corrected magnetic deflection system, the dynamic stigmator removes the spot ellipticity in all planes close to the image; as shown in figure 4.4 for a magnetic deflection system.

Contrary to the magnetic deflection system, here the spot retains its properties for lower deflections only. Astigmatism becomes considerable at $\delta_i = 200$–300 µm and the spot size actually decreases with increasing deflection as shown in table 5.2.

It was found that the chromatic aberrations has great effect in broadening the spot. Figure 5.5 shows the spot after correction of the field curvature, astigmatism, and distortion for the nominal energy $E_0 = 15$ keV and for energies $E_0 - dE/2$ and $E_0 + dE/2$, where $dE = 0.4$ eV. Rays with a slightly different energy form the spot at shifted positions. For deflections up to 200 µm the shift of the chromatic spot is less than 1/3 of the nominal energy spot diameter. In further studies it may be useful to find an optimal trade-off between probe size increase due to coma and chromatic aberration.

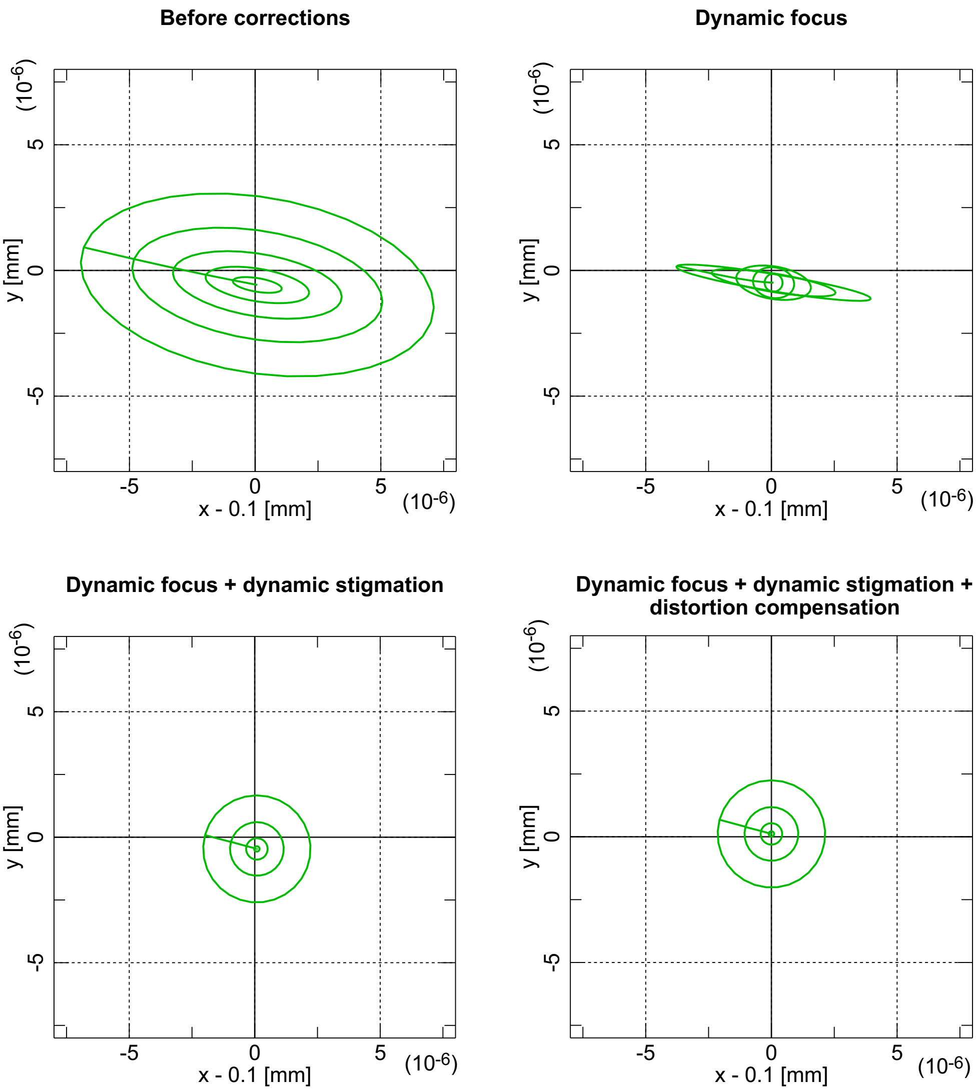

Figure 5.4: Change in 0.1 mm deflected spot size and shape after applying dynamic focus to eliminate field curvature (option IIIa), dynamic stigmation to eliminate deflection astigmatism, and distortion correction. The ellipses correspond to 5 equidistant initial ray angles up to the optimal aperture angle α_{opt}. The dynamic focus decreases the spot size in the sample plane, and the astigmatism correction compensates its ellipticity. The dynamic correction of distortion moves the spot to the paraxial deflection position within 0.1 nm which is around the tracing error level.

Table 5.2: The effect of deflection on spot size after dynamic corrections. The spot diameter was calculated for nominal beam energy.

Deflection [µm]	Write field [µm^2]	Major diameter [nm]	Minor diameter [nm]	Diameter increase %
0	N/A	4.4	N/A	0
100	140x140	4.3	N/A	-2
200	280x280	3.8	3.7	-15
300	420x420	3.5	3.1	-25
400	560x560	3.9	2.7	-25

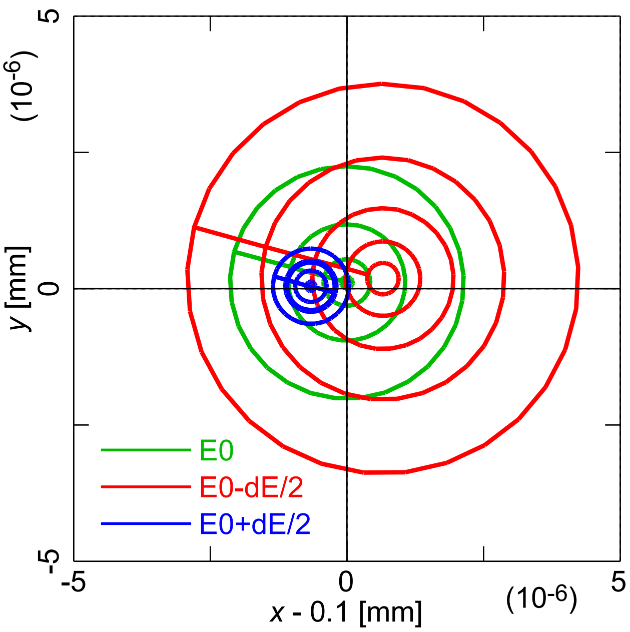

Figure 5.5: The effect of chromatic aberrations illustrated on a 0.1 mm deflected beam of energies close to the nominal energy 15 keV. The energy spread dE is 0.4 eV. The field curvature, astigmatism, and distortion are corrected. The circles correspond to 5 equidistant initial ray angles up to the optimal aperture angle α_{opt}.

5.6 Summary

In this chapter, the dynamic correction of the field curvature, astigmatism, and distortion of a newly designed electrostatic deflection system were studied. The electrostatic deflectors resemble the original magnetic ones in that they utilize two stages, they occupy the same space inside the objective lens bore, and have similar size. The deflectors consist of 8 equisectored electrodes, they do not produce a hexapole field, and share a voltage supply between the stages. The deflection system was optimized so that it had negligible coma. As chromatic aberration becomes significant, it may be useful in further studies to find an optimal trade-off between probe size increase due to coma and chromatic aberration by adjusting the rotation of the electrodes. A dynamic electrostatic stigmator was added to the setup just before the deflection system. The stigmator is also composed of 8 electrodes, and its quadrupole field was used to compensate deflection astigmatism. To eliminate field curvature, several methods and lenses have been proposed depending on the location of the dynamic focus lens. The optimal voltages of the dynamic correction devices, as well as their effect on distortion has been derived.

To demonstrate the functionality of the proposed dynamic corrections, they were implemented in the EOD model and their influence on spot size, shape, and position evaluated as shown in figure 5.4. The correction devices worked as expected for lower write fields up to around 250 µm^2. Decrease of the spot size and increase of ellipticity have been observed for higher deflections. A probable cause is that the derived formulas are sensitive to numerical errors and the found correction device voltages slightly differ from the optimal values. It was found that the spot becomes elliptical at 200–300 µm and higher deflections. The chromatic aberration has considerable effect on the spot properties by shifting the center of spots of slightly different energy and induces a 200 µm deflection limit according to the criterion discussed in section 5.5. For write fields used in electron-beam lithography applications at the Institute of Physical Engineering around 150×150 µm^2 the spot remains circular.

CONCLUSION

This thesis was focused on studying dynamic correction options in direct-write electron-beam lithography. The Tesla BS600 e-beam writer's optical column converted to Gaussian-beam mode was chosen to explore these possibilities. The goals of the thesis were to study the properties of the current magnetic deflection and dynamic focus system, and to design new electrostatic deflection and electrostatic aberration correction devices. The deflection aberrations treated in this thesis were: coma, field curvature, astigmatism, and distortion.

The first part of the thesis offers an introduction into the laws and relations governing charged particle optics (chapter 1), as well as some practical aspects of particle optics devices such as the design of lenses, beam deflectors, and stigmators. The fundamental paraxial approximation and aberration theory are described. A few pages of chapter 2 are devoted to electron-beam lithography; its evolution from the early ages up to the state-of-the-art concepts of recent years. A very short description of the electron-beam pattering process is given, and a few other techniques offering sub-micron or nanometer-scale pattering are listed. A short chapter 3 is dedicated to the Tesla BS600 series electron-beam writer the electron lenses of which have been used as the studied optical system. The changes needed to convert the shaped-beam writer to Gaussian-beam mode are described. The main part of the thesis is the study of the magnetic deflection and correction devices in chapter 4, and the design of an equivalent electrostatic system in chapter 5.

An EOD (Electron Optical Design) model of the lithography machine's optical components has been created and used extensively to evaluate its properties. The existing magnetic deflection system and dynamic focus coils compensating the field curvature have been supplemented with a dynamic stigmator to eliminate the deflection astigmatism. Multiple methods have been proposed to calculate the optimal excitation of these correction devices such as using EOD's focusing capabilities, fitting the necessary parameters, or deriving the sought terms using aberration theory. The methods were compared when possible, and the dynamic corrections implemented in the EOD model. The final result of the optimal aberration correction was demonstrated and its influence on the beam spot size and shape was shown.

A new electrostatic deflection system has been designed to replace the magnetic deflectors. Electrostatic multipoles offer higher deflection frequencies as they are not limited by induced eddy currents. An equisectored 8-electrode dual-stage deflection system was designed, optimized, and its aberrations were evaluated. Several electrostatic dynamic focusing options have been proposed to eliminate the deflection field curvature, differing in the placement of the unipotential correction lens. An 8-electrode electrostatic stigmator has been designed and implemented to compensate the deflection astigmatism. The effect of the newly introduced correction devices on distortion has been derived and compensated by superimposing a small correction onto the deflection signal. The functionality of the correction devices and the correctness of the aberration integrals derivation have been demonstrated on beam spots calculated by ray tracing.

The electrostatic deflection system has slightly higher field curvature, distortion, and chromatic aberration coefficients; of these, only the chromatic aberration cannot be corrected dynamically. Using dynamic correction devices, the achievable spot properties are similar for write fields up to $200\times200\ \mu m^2$ after which the electrostatically deflected beam becomes considerably elliptical. The magnetically deflected and corrected beam spot retains its properties up to a $1\times1\ mm^2$ write field. It was found that the correctors have no effect on distortion as long as the correction fields are situated before the deflectors. Formulas giving the influence of dynamic focus and stigmator fields on distortion in the general case have been derived and tested by ray tracing.

Dynamic correction of aberrations is an important aspect of direct-write electron-beam lithography as it can increase the most limiting factor of these machines in commercial applications— the throughput. The derived framework and results may be used in future designs of electron-beam lithography or microscopy systems.

BIBLIOGRAPHY

[1] P. Urban, "Zobrazení vlivu aberací v částicové optice," Master's thesis, Faculty of Mechanical Engineering, Brno University of Technology, Brno, 2001.

[2] B. Lencová, "Particle optics course notes," 2014, Faculty of Mechanical Engineering, Brno University of Technology, Brno.

[3] H. Rose, *Geometrical Charged-Particle Optics*, ser. Springer Series in Optical Sciences. Springer Berlin – Heidelberg, 2013.

[4] P. Hawkes and E. Kasper, *Principles of Electron Optics: Basic geometrical optics*, ser. Principles of Electron Optics. Academic Press, 1989.

[5] B. Lencová and J. Zlámal, *EOD (Electron Optical Design) v4.004 manual*, 2015.

[6] O. Scherzer, "Über einige fehler von elektronenlinsen," *Zeitschrift für Physik*, vol. 101, no. 9-10, pp. 593–603, 1936, as cited in Peter Hawkes – *The long road to spherical aberration correction*, 2001.

[7] "Coma (optics)," http://en.wikipedia.org/wiki/Coma_(optics), [Online] Accessed: 2015-05-18.

[8] P. W. Hawkes, "Aberrations," in *Handbook of Charged Particle Optics, Second Edition*, J. Orloff, Ed. CRC Press, 2009.

[9] L. Reimer, *Scanning Electron Microscopy: Physics of Image Formation and Microanalysis*, ser. Springer Series in Optical Sciences. Springer Berlin – Heidelberg, 1998.

[10] M. Horák, "Charakterizace elektronové trysky," Bachelor's thesis, Faculty of Mechanical Engineering, Brno University of Technology, Brno, 2013.

[11] B. Lencová, "Electrostatic lenses," in *Handbook of Charged Particle Optics, Second Edition*, J. Orloff, Ed. CRC Press, 2009.

[12] P. W. Hawkes, *Magnetic Electron Lenses*. Springer Berlin – Heidelberg, 1982.

[13] K. Tsuno, "Magnetic lenses for electron microscopy," in *Handbook of Charged Particle Optics, Second Edition*, J. Orloff, Ed. CRC Press, 2009.

[14] B. Lencová, "Metody elektronové optiky pro elektronovou litografii," CSc. dissertation, Institute of Scientific Instruments, Czech Academy of Sciences, Brno, 1988.

[15] B. Lencová and J. Zlámal, *EOD Finite Element Method manual*, 2013.

[16] X. Zhu, H. Liu, and E. Munro, "Dynamic correction of aberrations in focusing and deflection systems with shaped beams," in *SPIE's 1995 International Symposium on Optical Science, Engineering, and Instrumentation*. International Society for Optics and Photonics, 1995, pp. 66–77.

[17] J. Zlámal and B. Lencová, "Development of the program EOD for design in electron and ion microscopy," *Nuclear Instruments and Methods in Physics Research Section A: Accelerators, Spectrometers, Detectors and Associated Equipment*, vol. 645, no. 1, pp. 278–282, 2011.

[18] V. R. Manfrinato *et al.*, "Resolution limits of electron-beam lithography toward the atomic scale," *Nano Letters*, vol. 13, no. 4, pp. 1555–1558, 2013.

[19] D. W. Carr and R. C. Tiberio, "Direct-write electron beam lithography: History and state of the art," in *Symposia J/N – Materials Issues and Modelling for Device Nanofabrication*, ser. MRS Proceedings, vol. 584, 1999.

[20] R. Feynman, "There's plenty of room at the bottom [data storage]," *Microelectromechanical Systems, Journal of*, vol. 1, no. 1, pp. 60–66, 1992.

[21] T. H. P. Chang and W. C. Nixon, in *Record of the 9th Symposium on Electron Ion and Laser Beam Technology*, vol. 123, 1967.

[22] R. F. M. Thornley and M. Hatzakis, in *Record of the 9th Symposium on Electron Ion and Laser Beam Technology*, vol. 94, 1967.

[23] I. Haller, M. Hatzakis, and R. Srinivasan, "High-resolution positive resists for electron-beam exposure," *IBM Journal of Research and Development*, vol. 12, no. 3, pp. 251–256, 1968.

[24] E. D. Wolf *et al.*, "Response of the positive electron resist, Elvacite 2041, to kilovolt electron-beam exposure," in *Record of the 11th Symposium on Electron, Ion, and Laser Beam Technology*, 1971, pp. 331–336.

[25] H. C. Pfeiffer, "Recent advances in electron-beam lithography for the high-volume production of VLSI devices," *Electron Devices, IEEE Transactions on*, vol. 26, no. 4, pp. 663–674, April 1979.

[26] H. C. Pfeiffer, "Direct write electron beam lithography: a historical overview," in *Proc. SPIE*, vol. 7823, 2010.

[27] L. Harriott, "SCALPEL: projection electron beam lithography," in *Particle Accelerator Conference, 1999. Proceedings of the 1999*, vol. 1. IEEE, 1999, pp. 595–599.

[28] H. C. Pfeiffer, "PREVAIL: IBM's e-beam technology for next generation lithography," in *Microlithography 2000.* International Society for Optics and Photonics, 2000, pp. 206–213.

[29] Y. Sakitani *et al.*, "Electron-beam cell-projection lithography system," *Journal of Vacuum Science & Technology B*, vol. 10, no. 6, pp. 2759–2763, 1992.

[30] M. Yamabe, presented at SEMICON Japan 2009, as cited in H. C. Pfeiffer – *Direct write electron beam lithography: a historical overview*, 2010.

[31] S. Okazaki, “High resolution optical lithography or high throughput electron beam lithography: The technical struggle from the micro to the nanofabrication evolution,” *Microelectronic Engineering*, vol. 133, pp. 23–35, 2015.

[32] J. Babocký, “Optické vlastnosti asymetrických plasmonických struktur,” Master’s thesis, Faculty of Mechanical Engineering, Brno University of Technology, Brno, 2014.

[33] W. Zhou, *Nanoimprint Lithography: An Enabling Process for Nanofabrication*, ser. SpringerLink : Bücher. Springer Berlin – Heidelberg, 2013.

[34] S. Natarajan *et al.*, “A 14nm logic technology featuring 2nd-generation FinFET, air-gapped interconnects, self-aligned double patterning and a 0.0588µm^2 SRAM cell size,” in *Electron Devices Meeting (IEDM)*. IEEE, 2014, pp. 3–7.

[35] J. Roberts *et al.*, “Exposing extreme ultraviolet lithography at Intel,” *Microelectronic Engineering*, vol. 83, no. 4–9, pp. 672 – 675, 2006, Proceedings of the 31st International Conference on Micro- and Nano-Engineering.

[36] S. Cabrini and S. Kawata, *Nanofabrication handbook*. CRC Press, 2012.

[37] F. Matějka, *Servisní dokumentace k fyzikální části elektronového litografu BS601*, Institute of Scientific Instruments, Czech Academy of Sciences, 2006.

[38] V. Kolařík *et al.*, “Zápis tvarovaným elektronovým svazkem,” *Jemná mechanika a optika*, pp. 11–16, January 2008.

[39] H. Ohiwa, “Moving objective lens and the Fraunhofer condition for predeflection,” *Optik*, vol. 53, no. 1, pp. 63–68, 1979.

[40] O. Sháněl, J. Zlámal, and M. Oral, “Calculation of the performance of magnetic lenses with limited machining precision,” *Ultramicroscopy*, vol. 137, pp. 1–6, 2014.

[41] B. Lencová, “On the design of electron beam deflection systems,” *Optik*, vol. 79 (1), pp. 1–12, 1988.

[42] D. Ilić *et al.*, “Mechanisms of electrical breakdown in low vacuums,” *Scientific Publications of the State University of Novi Pazar Series A: Applied Mathematics, Informatics and mechanics*, vol. 3, no. 2, pp. 85–99, 2011.

[43] E. Weidlich, “Design of a non-equisectored 20-electrode deflector for e-beam lithography using a field emission electron beam,” *Microelectronic engineering*, vol. 11, no. 1, pp. 347–350, 1990.

[44] I. Vlček, “Teoretické a experimentální studium vlastností Wienova filtru pro použití v rastrovacím mikroskopu s velmi nízkou energií elektronů,” Ph.D. dissertation, Faculty of Mechanical Engineering, Brno University of Technology, Brno, 2005.

[45] P. W. Hawkes, “Asymptotic aberration integrals for quadrupole systems,” *Optik*, vol. 31, no. 4, p. 302, 1970.